

# Inter-annual global carbon cycle variations linked to atmospheric circulation variability

Na Li<sup>1</sup>, Sebastian Sippel<sup>2</sup>, Alexander J. Winkler<sup>1</sup>, Miguel D. Mahecha<sup>3</sup>, Markus Reichstein<sup>1</sup>, and Ana Bastos<sup>1</sup>

<sup>1</sup>Max Planck Institute for Biogeochemistry, Germany

<sup>2</sup>Institute for Atmospheric and Climate Science, and Seminar for Statistics, ETH Zurich, Switzerland

<sup>3</sup>Remote Sensing Center for Earth System Research, Leipzig University, Germany

**Correspondence:** Na Li (nali@bgc-jena.mpg.de)

## Abstract.

One of the least understood temporal scales of global carbon cycle (C-cycle) dynamics is its inter-annual variability (IAV). This variability is mainly driven by variations in the local climatic drivers of terrestrial ecosystem activity, which in turn are controlled by large-scale modes of atmospheric variability. Here, we quantify the fraction of global C-cycle IAV that is explained by large-scale atmospheric circulation variability, which is quantified by spatio-temporal sea level pressure (SLP) fields. C-cycle variability is diagnosed from the global detrended atmospheric CO<sub>2</sub> growth rate and the land CO<sub>2</sub> sink from 16 dynamic global vegetation models and two atmospheric inversions in the Global Carbon Budget 2018. We use a regularized linear regression model, a statistical learning technique apt to deal with the large number of atmospheric circulation predictors ( $p \geq 800$ , each representing one pixel-based time-series of SLP anomalies) in a relatively short observed record ( $n < 60$  years). We show that boreal winter and spring SLP anomalies allow predicting IAV in atmospheric CO<sub>2</sub> growth rate and of the global land sink, with Pearson correlations between reference and predicted values between 0.70–0.84 boreal winter SLP anomalies. This is comparable or higher than that of a similar model using 15 traditional teleconnection indices as predictors. The spatial patterns of regression coefficients of the model based on SLP fields show a predominant role of the tropical Pacific and over Southeast Asia extending to Australia, corresponding to the regions associated with the El Niño/Southern Oscillation variability. We also identify another important region in the western Pacific, roughly corresponding to the West Pacific pattern.

We further evaluate the influence of the time-series length on the predictability of IAV and find that reliable estimates of global C-cycle IAV can be obtained from records of 30–54 years. For shorter time-series ( $n < 30$  years), however, our results show that conclusions about CO<sub>2</sub> IAV patterns and drivers need to be evaluated with caution. Overall, our study illustrates a new data-driven and flexible approach to model the relationship between large-scale atmospheric circulation variations and C-cycle variability at global and regional scales, complementing the traditional use of teleconnection indices.

## 1 Introduction

The global carbon cycle (C-cycle) varies at multiple time scales ranging from minutes to millennium (Ciais et al., 2013). Quantifying and understanding the patterns of variability in the C-cycle and their drivers is crucial to better understand C-cycle

dynamics and better constrain future climate projections (Cox et al., 2013; Friedlingstein et al., 2014). Primarily driven by the  
25 land sink dynamics (Piao et al., 2020), inter-annual variability (IAV) is one of the most uncertain and poorly understood terms  
of the global C-cycle in the observational period (Friedlingstein et al., 2019).

A fundamental challenge is that variability in land-atmosphere carbon exchange is affected in complex ways by large-scale  
atmosphere circulation modes but also land use changes, forced climate changes, direct physiological CO<sub>2</sub> effects on ecosys-  
tems, among others (IPCC, 2013). Separating these effects is difficult because of the large uncertainties associated with some  
30 processes, for example land use change (Friedlingstein et al., 2022) or processes not directly observable at global scale (e.g.,  
photosynthesis or heterotrophic respiration) (Schimel et al., 2015; Basile et al., 2020). The second challenge is that the land  
sink, as a balance of carbon uptake and release, responds differently to variations in the climatic forcing (Jung et al., 2017; Piao  
et al., 2020). This makes it hard to attribute induced land sink IAV to specific drivers, which is crucial for process understand-  
ing (Jung et al., 2017; Humphrey et al., 2018, 2021; Wang et al., 2022). Last, the limited length of observational records may  
35 hamper robust statistical analysis (IPCC, 2013): the longest continuous observations of atmospheric CO<sub>2</sub> at the South Pole and  
Mauna Loa observatory exist only since 1958 onwards (Dlugokencky and Tans, 2019).

Land biospheric CO<sub>2</sub> uptake results from the net balance of carbon uptake from gross primary productivity, and release  
from multiple respiration terms, and disturbance induced fluxes such as fires, amongst other smaller terms (IPCC, 2013). Most  
of these processes are primarily driven by temperature, water and radiation availability (Jung et al., 2017). These meteoro-  
40 logical drivers are, in turn, modulated by large-scale modes of atmospheric circulation on multiple time-scales, such as El  
Niño/Southern Oscillation (ENSO; Gu and Adler, 2011) and the Pacific Decadal Oscillation (PDO; Newman et al., 2016).  
These climate variability modes are generated within the coupled atmosphere-ocean systems (Ghil, 2002) and considered ir-  
reducible noise in climate projections (Madden, 1976; Schneider and Kinter, 1994; Deser et al., 2012). Because these modes  
typically interact and affect weather dynamics in regions beyond those where they are emerged, such modes are collectively  
45 referred to as teleconnections (IPCC, 2013). Bacastow (1976) showed that ENSO is highly correlated with annual variations in  
observed atmospheric CO<sub>2</sub> measured at the South Pole and Mauna Loa, Hawaii. Keeling et al. (1995) attributed these correla-  
tions to the ENSO impact on the biospheric sink. In addition to ENSO, Zhu et al. (2017) showed that the PDO and the Atlantic  
Multi-decadal Oscillation (AMO; Enfield et al., 2001; Rayner et al., 2003) may also influence global terrestrial ecosystem  
carbon fluxes and that other modes of variability in the Northern Hemisphere have also local impacts on carbon cycling (Zhu  
50 et al., 2017).

A common approach to diagnose the impacts of natural climate variability is to use ensembles of Earth system model  
simulations with perturbed initial conditions to quantify the impacts of natural climate variability at decadal to millennium  
scales (Frölicher et al., 2013). However, the inherently chaotic atmosphere, in combination with model structural uncertainty,  
implies large uncertainties for future projections (Deser et al., 2020). Also, Earth system model projections can be compromised  
55 by limited representation of the full complexity of physical processes involved, lack of observational constraints, and high  
computational demands when aiming to resolve high resolutions (Randall et al., 2007; IPCC, 2013).

Statistical approaches are a simplified but effective way to reveal physical processes in observations (von Storch, 1995). A  
traditional approach consists of evaluating relationships between the variables of interest (e.g. CO<sub>2</sub> time-series) and telecon-

nection indices (Bacastow, 1976; Bastos et al., 2013; Zhu et al., 2017). As a simple representation of the large-scale atmospheric circulation modes, teleconnection indices are extracted mainly from sea surface temperature or atmospheric anomalies (Kumar and Hoerling, 1997; IPCC, 2013). Such indices are an effective way to reduce the complexity of the spatio-temporal variability in multiple variables (Stenseth et al., 2003; Wills et al., 2017), but may not be able to capture spatial variations in the large-scale atmospheric circulation modes themselves.

Recently, Sippel et al. (2019) applied Ridge Regression, a regularized linear regression method (Hastie et al., 2009; Friedman et al., 2010), to quantify the component of precipitation and temperature variability driven by atmospheric variations based on sea level pressure (SLP) fields, rather than teleconnection indices. Their approach allowed them to robustly infer the main spatio-temporal patterns of atmospheric variability influencing these two climate variables. On the one hand, including a field of circulation-based predictors, avoids considering predefined assumptions about their spatial configurations as they are common to teleconnection indices, while compensating for relatively short historical records. The regularization approach, on the other hand, allows to overcome overfitting and multicollinearity issues due to short time series and a very large number of spatial predictors.

In this study, we adopt the Ridge Regression approach in Sippel et al. (2019), aiming to quantify the fraction of global C-cycle IAV influenced by large-scale atmospheric circulation variability. We use observation-based time-series of global atmospheric CO<sub>2</sub> growth rate (*AGR*) and land CO<sub>2</sub> surface fluxes from atmospheric inversions and Dynamic Global Vegetation (DGVMs), as well as the land sink estimated as a residual of other terms in the Global Carbon Budget 2018 (Le Quéré et al., 2018). We first evaluate and compare the predictive skill of the Ridge Regression model when using SLP as predictors versus commonly used traditional teleconnection indices (Section 3.1). Next, we analyze and discuss how the global C-cycle sensitivity to atmospheric circulation variability from various latitudinal domains of SLP anomaly fields (Section 3.2). Finally, we evaluate the sensitivity of the results to the length of the time-series (Section 3.3), by comparing the fraction of C-cycle IAV that can be explained by large-scale atmospheric circulation variability based on these datasets with that of a very long time-series (4000 years) of land CO<sub>2</sub> fluxes simulated by the Community Earth System Model (CESM).

## 2 Data and methods

### 2.1 CO<sub>2</sub> datasets for the recent past

We select the CO<sub>2</sub> time-series datasets from the Global Carbon Budget 2018 version 1.0 (Le Quéré et al., 2018): the atmospheric CO<sub>2</sub> growth rate (*AGR*), the land sink from models (*SL*<sub>DGVMs</sub>), the residual land sink (*SL*<sub>Resid</sub>), and the land sink from two atmospheric inversions.

In the Global Carbon Budget 2018 (Le Quéré et al., 2018), the global CO<sub>2</sub> balance is calculated based on the carbon emissions from fossil fuel (*FF*) (Boden et al., 2017; UNFCCC, 2018; Peters et al., 2011b) and land use change (*FLUC*) (Houghton and Nassikas, 2017; Hansis et al., 2015), the *AGR* (Dlugokencky and Tans, 2018), the carbon uptake by the ocean sink (*SO*) and the land sink (*SL*) (references for individual models of *SO* and *SL* can be found in Table 4 of Le Quéré et al. (2018)).

The difference of annual atmospheric CO<sub>2</sub> in a given year and the previous year (Ballantyne et al., 2012; Dlugokencky and Tans, 2018; Le Quéré et al., 2018) corresponds to the *AGR*, which is based on direct observations. The *AGR* is based on the average of well-mixed CO<sub>2</sub> measurements at multiple global stations from the US National Oceanic and Atmospheric Administration Earth System Research Laboratory (NOAA ESRL) (Dlugokencky and Tans, 2018).

*FF* emissions are based on inventories, while *FLUC*, *SL* and *SO* are estimated by models (*SL*<sub>DGVMs</sub> and *SO*, respectively in Eq. (1), all of which contain uncertainties (Le Quéré et al., 2018). The total emissions from *FF* and *FLUC* minus *AGR* should equal the *SO* and *SL*<sub>DGVMs</sub> (Eq. (1)). Due to uncertainties in modeled land and/or ocean sinks or in land use estimations (Bastos et al., 2020; Hauck et al., 2020), the budget cannot be balanced and thus an imbalance term (*IMB*) is introduced to the budget.

$$FF + FLUC - AGR - SO = SL_{DGVMs} + IMB = SL_{Resid} \quad (1)$$

The annual land sink of CO<sub>2</sub> (*SL*<sub>DGVMs</sub>) is the average net biome production (NBP) simulated by 16 dynamic global vegetation models (DGVMs) forced with historical CO<sub>2</sub> and changing climate (Le Quéré et al., 2018). The residual land CO<sub>2</sub> (*SL*<sub>Resid</sub>) is calculated from emissions, *AGR*, and ocean sinks, as described in Eq. (1). *SL*<sub>Resid</sub> corresponds to the balance of the fossil fuel and land-use change emissions and the sinks in the atmosphere and ocean and provides an alternative estimate of the global land sink.

The time-series of *AGR*<sub>R</sub>, *SL*<sub>DGVMs</sub>, and *SL*<sub>Resid</sub> in Global Carbon Budget 2018 (Le Quéré et al., 2018) are provided at annual time-steps over the period 1959–2017. In the following analysis, we invert the *AGR* time-series (*AGR*<sub>R</sub> for reversed *AGR* i.e.  $-1 \times AGR$ ) for sign consistency with the land sink datasets used (defined as a positive flux from the atmosphere to the land).

Additionally, we use the globally aggregated net atmosphere to land CO<sub>2</sub> flux (positive sign as a sink in the biosphere) estimated from two atmospheric CO<sub>2</sub> inversions in Global Carbon Budget 2018 (Le Quéré et al., 2018): the Jena CarboScope *SL*<sub>CarboScope</sub> (Rödenbeck, 2005; Rödenbeck et al., 2018), and the Copernicus Atmosphere Monitoring Service inversion *SL*<sub>CAMS</sub> (Chevallier et al., 2005), which cover the periods 1976–2017 and 1979–2017 respectively. Here we use the global annual CO<sub>2</sub> fluxes of these two inversions adjusted for fossil fuel emissions and lateral fluxes from Bastos et al. (2020). The period common to the CO<sub>2</sub> time-series (1980–2017) is selected.

### 2.1.1 Sea level pressure

We use global monthly mean SLP fields from ERA5 reanalysis with the spatial resolution of  $0.25^\circ \times 0.25^\circ$  (Bell et al., 2020), at monthly time-steps and covering the period 1950–1978 (Bell et al., 2020) and 1979–present (Hersbach et al., 2019). The period common to other datasets of 1958–2017 is selected here.

### 2.1.2 Teleconnection indices

In addition to SLP fields, we select 15 teleconnection indices from the atmosphere–ocean variability, Northern Hemisphere, and Southern Hemisphere.

Three important atmosphere–ocean coupled variability modes influence global climate and the C–cycle: the El Niño–Southern  
125 Oscillation (SOI), the Pacific Decadal Oscillation (PDO), and the Atlantic Multidecadal Oscillation (AMO) (Zhu et al., 2017).

In the Northern Hemisphere, the most relevant indices are: the Arctic Oscillation (AO), the North Atlantic Oscillation (NAO),  
the Pacific North American pattern (PNA), the East Atlantic (EA), the East Atlantic/Eastern Russia (EAWR), the Scandinavian  
pattern (SCAND), the Polar/Eurasia (polarEA), and the West Pacific (WP). These indices are calculated and provided by the  
Climate Prediction Centre (CPC) of the National Oceanic and Atmospheric Administration (NOAA), and provided by the  
130 NOAA National climate prediction center (CPC, 2008). The detailed information on calculation procedures is described on  
NOAA CPC (2008) and Barnston and Livezey (1987).

In the Southern Hemisphere, important indices are the Antarctic Oscillation (AAO), the Tropical Atlantic Dipole (TAD), the  
Dipole Mode Index (DMI) of the Indian Ocean Dipole, and the Trans Polar index (TPI).

The teleconnection indices used here have been summarized in Table 1. All the indices are provided as monthly means and  
135 selected for the period of 1958–2017, except the AAO which is available for 1979–2017 only.

### 2.1.3 Long-term pre-industrial control simulations for statistical benchmarking

Here we select the SLP fields and global net biome production fields (NBP) from simulations by the Community Earth System  
Model (CESM) version 1.2.2 (in the B1850C5CN configuration), which has been used by Stolpe et al. (2019). This experiment  
corresponds to a 4000-yr control run. The simulation was run at an atmospheric resolution of  $1.9^{\circ} \times 2.5^{\circ}$ , using the Community  
140 Atmosphere Model version 5 (CAM5.3; (Neale et al., 2012)) with 30 vertical levels. The model consists of fully coupled  
atmosphere, ocean, sea ice and land surface components (Hurrell et al., 2013; Meehl et al., 2013b), and did not include dynamic  
vegetation. This simulation includes no external forcing, so it is ideal to analyze patterns driven by internal variability.

## 2.2 Data pre-treatment

For all historical datasets (CO<sub>2</sub> time-series, SLP fields and teleconnection indices), we first remove years corresponding to  
145 volcanic eruptions (1963, 1982, 1983, 1991, 1992). We then pre-treat the datasets as follows.

### 2.2.1 Trend removal

The long-term trend of CO<sub>2</sub> time-series is removed by locally weighted scatterplot smoothing (LOWESS) (Cleveland et al.,  
1991) of the annual time-series with fixed window size of 25 % interval longer than 30 years (1959–2017) and 45 % for shorter  
period (1980–2017). For monthly teleconnection indices, we first calculate the seasonal mean values of DJF, MAM, JJA, and  
150 SON, we then remove the seasonal long-term trends by applying the LOWESS as for the CO<sub>2</sub> time-series, and further include  
DJF and MAM combined (DJF+MAM) as treated in SLP (as described below).

### 2.2.2 Spatial and temporal aggregation

The monthly mean SLP fields are area-weighted and aggregated to  $2^\circ \times 2^\circ$ ,  $5^\circ \times 5^\circ$ , and  $9^\circ \times 9^\circ$  spatial resolution, and the seasonal cycle removed by subtracting the monthly mean values for each pixel. We then aggregate SLP values in seasonal means for: December of the previous year to February of each given year (DJF), March–May (MAM), June–August (JJA), and September–November (SON) and further consider DJF and MAM combined (DJF+MAM), so the number of pixel-based time-series (predictors) in DJF+MAM is double of DJF. Note that a large fraction of the pixel-based time-series of seasonal SLP anomalies show no long-term trend, and the predicted differences between LOWESS detrended and not detrended SLP are small. Here we keep the analysis of SLP anomalies with no LOWESS detrending. Here, we refer to DJF and MAM as boreal winter and boreal spring.

For the CESM simulations, the SLP fields are originally provided at  $1.9^\circ \times 2.5^\circ$  spatial resolution at monthly mean time-steps, which we then resample to  $5^\circ \times 5^\circ$  spatial resolution. Annual mean NBP is calculated from the monthly fields. NBP and SLP fields are selected for the simulation period 1000–5000 year.

### 2.3 Statistical analysis

The overall goal is to characterize annual variations in the global C-cycle that can be explained by large-scale atmospheric circulation variability. Here, the pixel-based time-series of SLP anomalies are used as predictors ( $p \geq 800$ ) of  $\text{CO}_2$  time-series ( $n \leq 54$  years) in a linear regression model. However, the small sample size relative to the large number of predictors ( $n < p$ ) can cause severe overfitting problems and result in unstable predictions (Hastie et al., 2009). Moreover, the existing spatial correlations among the neighboring pixels of SLP anomalies might cause multicollinearity among the predictors (von Storch and Zwiers, 1999). The potential multicollinearity problem results in unstable Ridge Regression coefficients in least square estimation, and making it difficult to diagnose the most sensitive spatial patterns of predictors (von Storch and Zwiers, 1999).

Sippel et al. (2019) applied Ridge Regression to avoid these overfitting and multicollinearity problems. Ridge Regression is a regularized linear regression, whose the fundamental principle is to introduce a constraint (hyper-parameter  $\lambda$ ) to regularize the varying regression coefficients in least squares estimation (Hastie et al., 2009; Friedman et al., 2010). The regularized variance comes with a compromise of biased predictions and is addressed as the bias-variance trade-off (Hastie et al., 2009). When selecting the best hyper-parameter  $\lambda$ , this trade-off is considered to achieve stable (low variance) while slightly biased predictions (Hastie et al., 2009).

Model performance is evaluated by the  $R^2$ , the Pearson's correlation  $R$ , and mean squared error of the original  $\text{CO}_2$  time-series against predicted values. Pearson's correlation  $R$  is selected as the main measure of predictability, and the significance  $P < 0.05$  is selected. Given the relatively short period ( $n < 60$ ), here we use leave-one-out cross-validation to achieve optimal model training and testing. For each train and test group splitting, we select the train group as all years excluding three consecutive years and the middle year of those three is then selected as the test sample. We exclude the preceding and following years to reduce the potential influence of temporal auto-correlation.

**Table 1.** Teleconnection indices

Index	Name	Description	Source
SOI	Southern Oscillation	Monthly sea level pressure anomalies differences (based on 1981–2010 monthly mean) between Tahiti and Darwin, Australia. (McBride and Nicholls, 1983; Ropelewski and Jones, 1987) Downloaded from the NOAA National centers for Environmental Information (NCEI).	<a href="https://www.ncdc.noaa.gov/teleconnections/enso/indicators/soi/#soi-calculation">https://www.ncdc.noaa.gov/teleconnections/enso/indicators/soi/#soi-calculation</a>
PDO	Pacific Decadal Oscillation	Monthly sea surface temperature (SST) variations in the Northeast and tropical pacific Ocean (Mantua et al., 1997; Mantua and Hare, 2002). Using EOF and regression over 20°–90° N in the Pacific (Mantua et al., 1997). Downloaded from NOAA NCEI.	<a href="https://www.ncdc.noaa.gov/teleconnections/pdo/">https://www.ncdc.noaa.gov/teleconnections/pdo/</a>
AMO	Atlantic multi-decadal Oscillation	Monthly Northern Atlantic temperature fluctuations (Rayner et al., 2003; Enfield et al., 2001). Computed by NOAA Physical Science Laboratory (PSL) (using Kaplan SST V2 dataset) from 0°–70° N (Enfield et al., 2001). The detrended and unsmoothed version is selected.	<a href="https://psl.noaa.gov/gcos_wgsp/Timeseries/AMO/">https://psl.noaa.gov/gcos_wgsp/Timeseries/AMO/</a>
AO	Arctic Oscillation	Characterized by winds circulations near the Arctic around 55° N. Calculated by NOAA NCEI, using Empirical Orthogonal Function (EOF) analyzes the monthly mean 1000 millibar height variations over 20°–90° N (Higgins et al., 2000, 2002).	<a href="https://www.ncdc.noaa.gov/teleconnections/ao/">https://www.ncdc.noaa.gov/teleconnections/ao/</a>
NAO	North Atlantic Oscillation	The Subtropical High and the Subpolar Low difference in sea level pressure (Barnston and Livezey, 1987). Downloaded from NOAA NCEI.	<a href="https://www.ncdc.noaa.gov/teleconnections/nao/">https://www.ncdc.noaa.gov/teleconnections/nao/</a>
PNA	Pacific-North America	Low–frequency Variations in the Northern Hemisphere extratropics (Barnston and Livezey, 1987; Chen and Van den Dool, 2003). Downloaded from NOAA NCEI.	<a href="https://www.ncdc.noaa.gov/teleconnections/pna/">https://www.ncdc.noaa.gov/teleconnections/pna/</a>
EA	East Atlantic	North–south dipole anomalies extending from the east to west North Atlantic, with a similar spatial structure to NAO (Barnston and Livezey, 1987).	<a href="https://www.cpc.ncep.noaa.gov/data/teledoc/ea.shtml">https://www.cpc.ncep.noaa.gov/data/teledoc/ea.shtml</a>
EAWR	East Atlantic/Western Russia	Distinct by four dominant anomaly centers with positive phase extending Europe and Northern China, negative covering central North Atlantic and North Caspian Sea (Barnston and Livezey, 1987).	<a href="https://www.cpc.ncep.noaa.gov/data/teledoc/eawruss.shtml">https://www.cpc.ncep.noaa.gov/data/teledoc/eawruss.shtml</a>
SCAND	Scandinavia	A main anomaly center over Scandinavia, and a opposite weaker sign over western Europe and eastern Russia/western Mongolia (Barnston and Livezey, 1987).	<a href="https://www.cpc.ncep.noaa.gov/data/teledoc/scand.shtml">https://www.cpc.ncep.noaa.gov/data/teledoc/scand.shtml</a>
PolarEA	Polar/Eurasia	In positive pattern, negative height anomalies in polar region, and positive anomalies in Northern China and Mongolia (Barnston and Livezey, 1987).	<a href="https://www.cpc.ncep.noaa.gov/data/teledoc/poleur.shtml">https://www.cpc.ncep.noaa.gov/data/teledoc/poleur.shtml</a>
WP	West Pacific	Low frequency variability of North Pacific (Barnston and Livezey, 1987).	<a href="https://www.cpc.ncep.noaa.gov/data/teledoc/wp.shtml">https://www.cpc.ncep.noaa.gov/data/teledoc/wp.shtml</a>
AAO	Antarctic Oscillation	Empirical Orthogonal Function (EOF) was applied to the monthly mean 700hPa height anomalies over 20°–90° S (Mo, 2000). Calculated by NOAA (CPC, 2008).	<a href="https://www.cpc.ncep.noaa.gov/products/precip/CWlink/daily_ao_index/ao/aoa.shtml">https://www.cpc.ncep.noaa.gov/products/precip/CWlink/daily_ao_index/ao/aoa.shtml</a>
TAD	Tropical Atlantic Dipole	Here we use TSA (Tropical Southern Atlantic Index). Obtained from NOAA Physical Sciences Laboratory (PSL), computed from the monthly SST average anomaly from 0°–20° S and 10° E–30° W, HadISST and NOAA OI 1x1 datasets are used (Enfield et al., 1999; Reboita et al., 2021).	<a href="https://psl.noaa.gov/data/correlation/tsa.data">https://psl.noaa.gov/data/correlation/tsa.data</a>
DMI	Dipole Mode	Obtained from NOAA PSL, based on the sea surface temperature anomaly gradient between the western and the South eastern equatorial Indian Ocean, HadISST1.1 SST is used (Saji and Yamagata, 2003; Reboita et al., 2021).	<a href="https://psl.noaa.gov/gcos_wgsp/Timeseries/Data/dmi.had.long.data">https://psl.noaa.gov/gcos_wgsp/Timeseries/Data/dmi.had.long.data</a>
TPI	Trans Polar	Normalized pressure difference between stations in Hobart and Stanley, Australia (Pittock, 1980, 1984; Jones et al., 1999), data calculated by Henley et al. (2015), data from University of East Anglia <a href="http://www.cru.uea.ac.uk/cru/data/tpi/">http://www.cru.uea.ac.uk/cru/data/tpi/</a> .	<a href="https://psl.noaa.gov/gcos_wgsp/Timeseries/TPI/">https://psl.noaa.gov/gcos_wgsp/Timeseries/TPI/</a>

185 A schematic description of the workflow from model training, validation and selection with the selected interval 1959–2017 is shown in Fig. 1. In panel (a), the global maps represent an example of the spatial distribution of SLP with a resolution of  $m^\circ \times m^\circ$ , where  $m$  varies in [2, 5, 9]. Each pixel corresponds to a time–series of SLP, so that  $p$  predictors ( $x_i$ , for  $i$  in 1~800)



with  $n = 54$  time-steps are defined. Each predictor is assigned a coefficient  $\omega_i$  to collectively predict CO<sub>2</sub> time-series  $Y$ , with length  $n = 54$ . The cost function (Harrington, 2012) is the sum of all the squared errors of training  $y_i$  minus estimated  $y'_i$  ( $x_i^T \omega$ ,  $\omega$  represents the vector of all  $\omega_i$ ). At the same time, the constraint function (Harrington, 2012) suppresses the coefficient variations under a regularized range defined by the hyper-parameter  $\lambda$ . Panel (b) shows the model training and validation processes. In this study, DJF SLP is aggregated to  $9^\circ \times 9^\circ$ , so  $p = 800$ . Note that to reduce the heavy computation load, when conducting spatial and temporal sensitivity study as described in Section 2.4, the range of  $\lambda$  is lower and with smaller steps than the range and step shown in the Panel (b). For example, when only selecting the tropical domain of SLP, the number of predictors is much less than 800. So the  $\lambda$  is selected in range  $[10, 1000]$  with a step of 50. When using teleconnection indices instead of SLP anomalies, the predictors are equal or less than 15, the range of  $\lambda$  is selected from  $[1, 200]$  with a step of 2.

The first step is to divide datasets into train and test groups, as shown in panel (c). The grouped training datasets are then used for model training and tune the best  $\lambda$  through 5-folds cross-validation, the best  $\lambda$  that achieves the optimal prediction (highest  $R^2$ ) is then selected by the model to predict test datasets. The model then starts another iteration with train and test grouping. Panel (c) describes the leave-one-out train and test grouping, the years before and after the selected test year are removed for each grouping to reduce the impact of temporal auto-correlations in CO<sub>2</sub> time-series.

Ridge Regression leave-one-out cross-validation is performed using the Python package Scikit-learn "Ridge" and the  $\lambda$  is tuned by Scikit-learn "RidgeCV" (Pedregosa et al., 2011). The global maps (Fig. 3, Fig. A4, Fig. A11, Fig. A12) are plotted by Cartopy (Met Office, 2010–2015).

## 2.4 Experimental design

1. Preliminary dependency tests. To evaluate the robustness of the results for different characteristics of the datasets and methodological choices, we perform several preliminary tests. **1)** Resolution-dependency test: evaluate the sensitivity of results to the SLP spatial resolution under  $2^\circ \times 2^\circ$ ,  $5^\circ \times 5^\circ$ , and  $9^\circ \times 9^\circ$ ; **2)** Seasonality-dependency test: evaluate the dependence of results on the definition of particular seasons, with each season being the combination of three consecutive months (from November last year to July the given year). **3)** Temporal auto-correlation of the CO<sub>2</sub> time-series: to ensure no significant trend remains in the detrended CO<sub>2</sub> time-series.

Here we directly use the results following the preliminary dependency test (Appendix A). The spatial resolution does not influence the results considerably (see Appendix A Fig. A1), therefore we select  $9^\circ \times 9^\circ$  SLP spatial resolution given its smaller number of grid points. The seasonal dependency test shows that DJF and MAM are seasonal combinations more representative of boreal winter and spring (see Appendix A Fig. A2). JJA and SON are found to have lower or no predictability to CO<sub>2</sub> time-series, therefore, we limit our results to DJF and MAM. As shown in Appendix A Fig. A3, the temporal auto-correlation of all CO<sub>2</sub> time-series is mostly less than 0.4 with lag ranging from 1 to 35 years. With a lag of one year, absolute values of auto-correlation are below 0.2, so that we can exclude strong temporal auto-correlation effects.



2. Model training and evaluation. We evaluate the predictability of annual CO<sub>2</sub> time-series using SLP anomalies, tele-  
220 connection indices, and SOI independently in the DJF, MAM, and DJF+MAM seasons, using the approach described  
above. We compare Pearson's correlation of observations and predicted values for different periods (1959–2017 and  
1980–2017) (Fig. 2 b) and show the corresponding Ridge Regression coefficient distribution maps (Fig. 3 a).
3. Spatial sensitivity study. We evaluate the predictability of historical annual CO<sub>2</sub> time-series using DJF SLP anomalies  
under different spatial domains in periods of 1959–2017 and 1980–2017. Then we use a 30-yr sliding window with  
225 annual  $AGR_R$  to depict how the predictability under various SLP domains evolves in the period 1959–2017.
4. Temporal sensitivity study. We evaluate the predictability of annual CO<sub>2</sub> time-series  $AGR_R$ ,  $SL_{DGVMs}$ , and CESM  
using DJF and MAM SLP anomalies under different time intervals. Sliding windows are employed at time intervals of  
15, 20, 30, 40 years for historical datasets and CESM, and 100, 500, and 2000 years for CESM only. For the interval of  
100 and 500 years, we use the sliding window of a 50 year step, and a 500 year step for the 2000 years interval. The  
230 intervals shorter than 100 years are all in 1 year step. We also evaluate the error rate of the model in each sliding window  
of 15, 20, 30, and 40 year lengths. The error rate is calculated by the number of invalid predictions that have significance  
 $P > 0.05$  divided by the number of total predictions within a given window.

### 3 Results and discussion

#### 3.1 Global IAV patterns

235 In this section, we test the predictability of the global C-cycle IAV by using different predictors: global SLP fields by Ridge  
Regression, teleconnection indices by Ridge Regression, and the single SOI index by simple linear regression. In this context,  
each detrended annual CO<sub>2</sub> time-series (including  $AGR_R$ ,  $SL_{Resid}$ ,  $SL_{DGVMs}$ ,  $SL_{CAMS}$ , and  $SL_{CarboScope}$ ) is predicted  
by the above predictors over DJF, MAM, and DJF+MAM separately (Fig. 2). The predictability is evaluated by the Pearson  
correlation ( $\rho$ ) between the original and predicted detrended annual CO<sub>2</sub> time-series.  $\rho_{SLP}$ ,  $\rho_{Tele}$ , and  $\rho_{SOI}$  represent the  
240 predictability by using different predictors of global SLP fields, teleconnection indices, and SOI respectively. Accordingly, the  
relevant Ridge Regression coefficients with above different predictors are represented as  $\omega_{SLP}$ ,  $\omega_{Tele}$ , and  $\omega_{SOI}$ .

First, we find the detrended annual CO<sub>2</sub> time-series are generally consistent with each other, except the  $SL_{DGVMs}$  shows  
slight deviation (Fig. 2 a). We find two anomalous years (1987 and 1998), which show deviations larger than 2 standard  
deviations in most CO<sub>2</sub> time-series, both signifying apparent  $AGR$  increases and subsequent lower land sink (Fig. 2 a). These  
245 two years correspond to strong El Niño events, which are usually associated with below-average land CO<sub>2</sub> uptake (Keeling  
et al., 1995; van der Werf et al., 2004; Bonan, 2016).

Global SLP and teleconnection indices show comparable predictive skill of global C-cycle IAV in winter, while teleconnec-  
tion indices have higher predictive skill in spring (Fig. 2 b). In both periods, the value of  $\rho_{SLP}$  (except  $SL_{DGVMs}$ ) is higher  
in DJF (0.51–0.70) than in MAM (0.29–0.60). On the other hand, the values of  $\rho_{Tele}$  are higher in MAM (0.57–0.79) than in

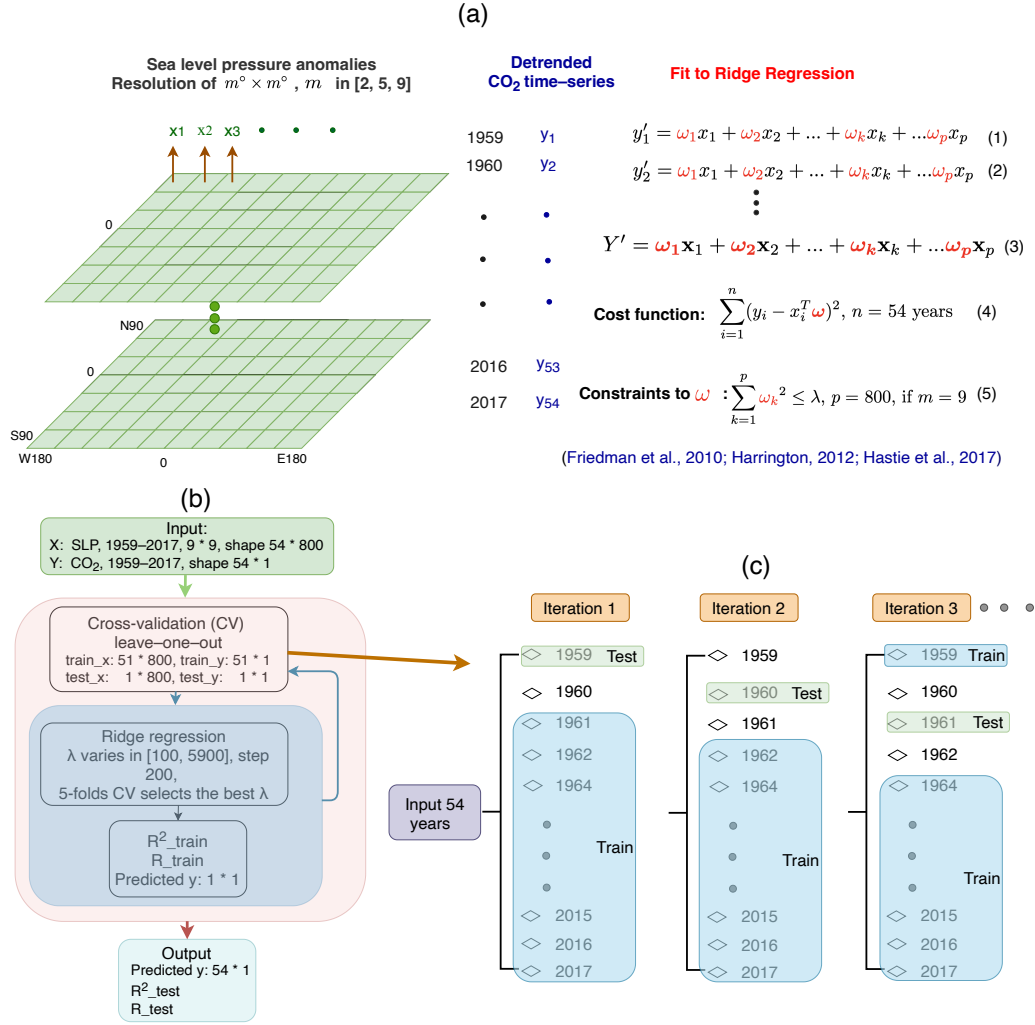


**Figure 1.** Schematic representation of the statistical approach and model design, with an example of the selected time interval of 1959–2017. (a) Fundamental principle of Ridge Regression. (b) Model training and validation under Ridge Regression leave-one-out cross-validation. (c) Train and test grouping through leave-one-out.

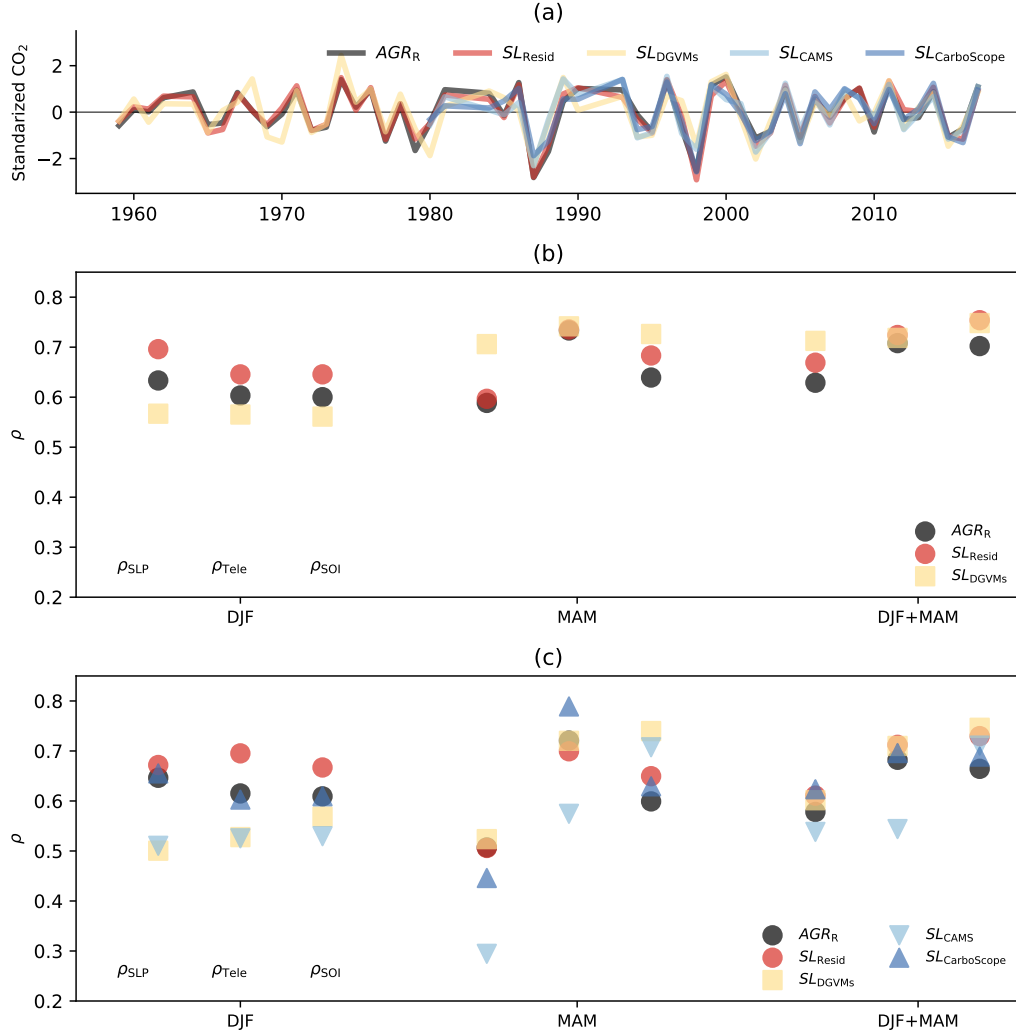


**Figure 2.** (a) Standardized annual observed/modeled CO<sub>2</sub> time-series over period 1959–2017 ( $AGR_R$  in black,  $SL_{Resid}$  in red and  $SL_{DGVMs}$  in yellow), and in period 1980–2017 ( $SL_{CAMS}$  in light blue and  $SL_{CarboScope}$  in dark blue). The CO<sub>2</sub> time-series have all been detrended as described in Section 2. Note that the  $AGR_R$ ,  $SL_{Resid}$ , and  $SL_{DGVMs}$  in period 1980–2017 are detrended data based on their relevant period, and compared with detrended data based on 1959–2017, the difference is negligible. (b) Pearson correlation of predicted vs observed/modeled CO<sub>2</sub> time-series based on the Ridge Regression with SLP fields ( $\rho_{SLP}$ ) or teleconnection indices ( $\rho_{Tele}$ ) as predictors. Additionally, Pearson correlation of predicted vs observed/modeled CO<sub>2</sub> time-series by linear regression is based on the single predictor of SOI index ( $\rho_{SOI}$ ). SLP fields, teleconnection indices, and SOI are aggregated for different seasons: DJF, MAM, and DJF+MAM. Panel (b) shows results for 1959–2017 and panel (c) for 1980–2017. Note that in panel (c), the  $\rho_{SLP}$  of  $SL_{CAMS}$  using MAM SLP as predictor has significance  $P = 0.09$ , all others have significance  $P < 0.05$ .

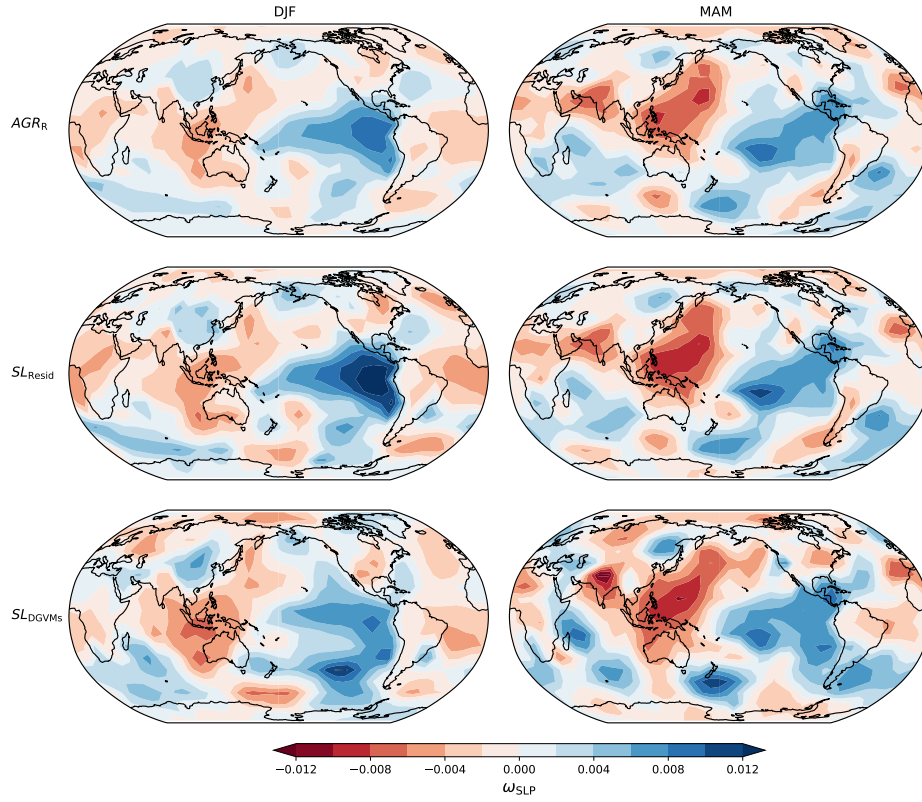
250 DJF (0.53–0.70). The relative low predictive skill of global SLP anomalies compared to teleconnection indices might result from: 1) limited sample size (less than 60 years) and a large number of predictors ( $p = 800$ ) for Ridge Regression training with global SLP anomalies. But for teleconnection indices and SOI, the predictability skills are much less influenced by the limited sample size due to their limited predictors ( $p \leq 15$  for teleconnection indices and  $p = 1$  for SOI). As we increase the sample size to over 100 years, the predictive skill of SLP anomalies increases considerably, as is shown in temporal sensitivity study (Fig. 6), and 2) the predictive skill of SLP anomalies in explaining global C-cycle IAV can be reduced in domains with large local rather than global impacts of atmospheric variations to land carbon sinks (Jung et al., 2017). In such domains, the SLP anomalies might show strong relationship to local C-cycle variations but weaker link to global C-cycle variations. Selecting the SLP domains with higher contribution to the global C-cycle variability could improve the predictability, as is shown by the analyzes of sensitivity of the results to the SLP spatial domains (Fig. 4).

260 Compared to the predictive skill of teleconnection indices, which includes a set of 14 teleconnection indices for period 1959–2017 and 15 for period 1980–2017 as predictors, the predictive skill of SOI is slightly lower or similar in both seasons, with 0.53–0.67 in DJF and 0.60–0.74 in MAM (Fig. 2 b). This is consistent with the dominant role of ENSO in driving global C-cycle IAV, with other modes showing less contributions. Such interpretation requires caution as the indices cannot fully represent the complex atmospheric dynamics.

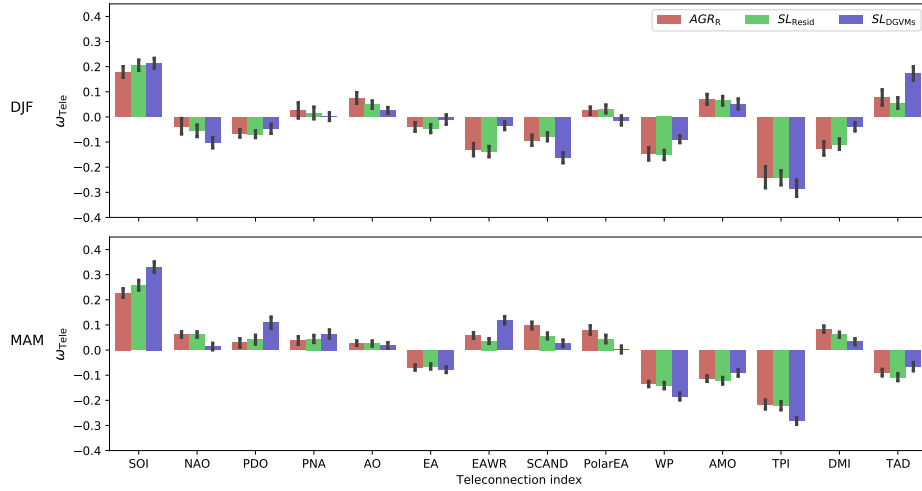
265 The predictive skill of the combined winter and spring global SLP anomalies reveal the different seasonal responses of global C-cycle IAV to large-scale atmospheric circulation variability (Fig. 2 b). The predictive skill of SLP and teleconnection indices in DJF+MAM is within the values for DJF and MAM for most datasets, and slightly higher than the best performing season for the predictive skill of SOI.

The predictive skill of SLP to  $SL_{\text{Resid}}$  is similar to  $SL_{\text{DGVMs}}$  in MAM and slightly higher than  $SL_{\text{DGVMs}}$  in DJF. The difference in the predictive skill of SLP to  $SL_{\text{Resid}}$  and  $SL_{\text{DGVMs}}$  in DJF may due to: 1) compared to  $SL_{\text{Resid}}$ , land sink IAV simulated by DGVMs is less sensitive to DJF climate forcing (Bastos et al., 2018), 2)  $SL_{\text{Resid}}$  implicitly includes the variability from land use change as well as ocean sink variations (Dufour et al., 2013; DeVries et al., 2017; Friedlingstein et al., 2019).

We next compare the spatial patterns of the Ridge Regression coefficients of SLP and teleconnection indices in the period of 1959–2017, the results of the period 1980–2017 can be found in Appendix A Fig. A4 and A5. The spatial patterns of the  $\omega_{\text{SLP}}$  are similar for the three CO<sub>2</sub> time-series: positive coefficients over eastern tropical Pacific Ocean and negative coefficients from Southeast Asia extending to Australia that together roughly consistent with ENSO, and negative from west Pacific (Fig. 3 a). In winter the positive coefficients over the eastern tropical Pacific are higher than in other regions, which are influenced by El Niño and La Niña respectively (Monahan, 2001; Hsieh, 2004; Rodgers et al., 2004; Schopf and Burgman, 2006; Sun and Yu, 2009; Yu and Kim, 2011): El Niño induces negative SLP anomalies over the East Pacific and positive SLP anomalies over the west Pacific (see King et al. (2020), Fig. 5). The results are consistent with the land sink being negatively driven by ENSO in winter: strong El Niño, decreased land sink, strong La Niña, increased land sink. In spring, the area over the central and western tropical Pacific also shows stronger coefficients, and likely corresponds to a mix of different modes, such as the ENSO, West Pacific teleconnection and the Interdecadal Pacific Oscillation, all showing strong coefficients in Fig. 3 b (SOI,



(a)



(b)

**Figure 3.** (a) Distribution of Ridge Regression coefficients of SLP with the time-series of  $AGR_R$  (top row),  $SL_{Resid}$  (center row) and  $SL_{DGVMs}$  (bottom row) in DJF (left column) and MAM (right column) based on SLP fields in the period 1959–2017. (b) Distribution of Ridge Regression coefficients of teleconnection indices with  $AGR_R$ ,  $SL_{Resid}$  and  $SL_{DGVMs}$ . Both  $\omega_{SLP}$  and  $\omega_{Tele}$  are the mean of the  $n = 54$  run Ridge Regression coefficients.

WP and TPI indices). In Fig. A11 we show the anomalies in temperature and precipitation associated to these patterns, as well as those in NBP from the two atmospheric inversions (Fig. A12). Generally, the temperature anomalies over the tropics show negative correlations to annual land sink (SLP driven  $AGR_R$ ) in both winter (as high as  $-0.85$ ) and spring (as high as  $-0.73$ ), while weaker but positive correlations are found in Eurasia. Tropical precipitation anomalies show roughly positive correlations in winter (as high as  $0.73$ ) and in spring (as high as  $0.67$ ). This pattern indicates that  $AGR_R$  is generally higher for cooler and wetter conditions over the tropics and Southern Hemisphere semi-arid regions in both seasons, which result in increased NBP (Fig. A12), as well as cooler but predominantly drier conditions over Eurasia, which result in a complex pattern of NBP anomalies (Fig. A12). These results are consistent with the strong ENSO fingerprint on the IAV of global  $CO_2$  atmospheric growth rate and global land sink, e.g. as pointed out by Piao et al. (2020) and with the importance of southern semi-arid ecosystems (Ahlström et al., 2015), for IAV in the global land sink.

The higher Ridge Regression coefficients of teleconnection indices are consistent with the high sensitivity domains of the Ridge Regression coefficients of SLP corresponding to the patterns of ENSO and WP (Fig. 3 b). Our results show that C-cycle IAV reveals a high positive sensitivity to SOI ( $0.18$  to  $0.21$ ) and negative sensitivity to TPI ( $-0.24$  to  $-0.28$ ) and WP ( $-0.09$  to  $-0.15$ ) in winter. High sensitivities are also found for DMI in winter (negative) and AMO in spring (negative) (Fig. 3 b). We find that the global C-cycle IAV is very sensitive to TPI as well as SOI, which is not so obvious for the spatial patterns of SLP Ridge Regression coefficients. TPI is a hemispheric-scale index and defined as the pressure anomaly differences between the locations Hobart ( $43^\circ$  S,  $147^\circ$  E) and Stanley ( $52^\circ$  S,  $58^\circ$  W) (Pittock, 1980, 1984). We find the TPI to be strongly anti-correlated with SOI in winter and spring ( $-0.89$  and  $-0.85$ , respectively). This might indicate an amplification of ENSO impacts on C-cycle IAV due to large-scale atmospheric circulation variability in the Southern Hemisphere.

However, the observed patterns of the Ridge Regression coefficients in teleconnection indices and SLP need to be interpreted with caution, since these patterns are not necessarily independent from each other. For example, the area from Southeast Asia extending to Australia corresponds to a region influenced by several large-scale atmospheric circulation modes: ENSO, the Indian Ocean Dipole (IOD), and the Southern Annular Mode (SAM) (Cleverly et al., 2016). Interactions between these modes have been shown to modulate the occurrence of drought and extreme precipitation in semi-arid areas of Australia, and thus induce large inter-annual variability in gross primary productivity in the region (Cleverly et al., 2016).

Compared to other  $CO_2$  datasets, the predictability of  $SL_{DGVMs}$  is higher when using SLP fields in MAM as predictors, rather than DJF (Fig. 2 b). Moreover,  $\omega_{SLP}$  of  $SL_{DGVMs}$  exhibits distinct spatial patterns, especially in winter, where  $\omega_{SLP}$  for  $SL_{DGVMs}$  show higher values in the Southern Pacific rather than over the tropical Pacific region (Fig. 3 a). Compared to historical results, predictability of  $SL_{DGVMs}$  is lower by using winter SLP as predictors in Ridge Regression, rather than by using spring SLP, and the spatial patterns of the Ridge Regression coefficients for  $SL_{DGVMs}$  are slightly different. These differences might be an indication of shortcomings of DGVMs in simulating the sensitivity of land sink to climatic drivers.

The general match of spatial patterns of the Ridge Regression coefficients using SLP and the teleconnection indices as predictors of global C-cycle IAV indicates that SLP can capture the spatial distribution of the atmospheric patterns that influence IAV, with the advantage of being more flexible than teleconnection indices, since it does not require predefined definitions. However, the short sample size and the large number of predictors for Ridge Regression training hinder the performance of

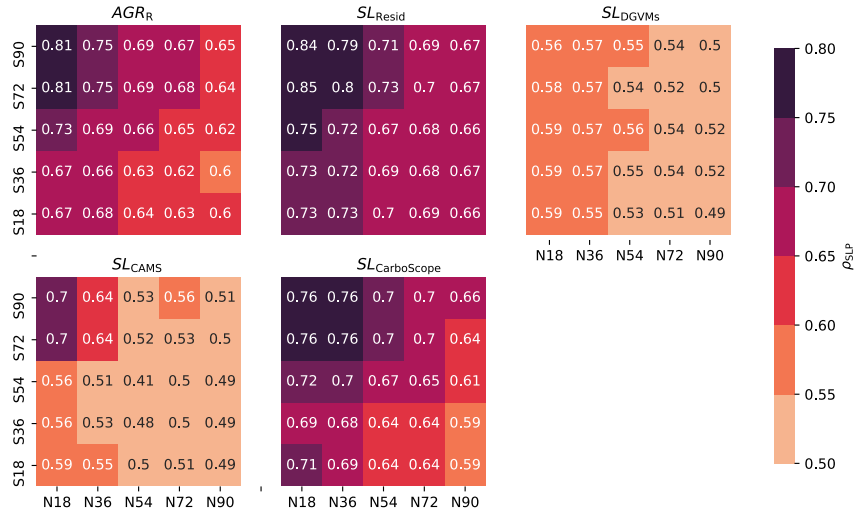


**Figure 4.** Heat map of predictability with CO<sub>2</sub> time-series over various SLP latitude domains in DJF. Each heat map contains 5×5 squares, and each square represents one domain of SLP. For example, the square 36° N–72° S is the domain of SLP extending from 36° N extending to 72° S. All latitudinal domains include the tropical area (18° N–18° S). The top right square thus represents global scale SLP.  $\rho_{SLP}$  of  $AGR_R$ ,  $SL_{Resid}$ ,  $SL_{DGVMs}$ ,  $SL_{CAMs}$ , and  $SL_{CarboScope}$  in 1980–2017 are shown here.

320 SLP anomalies, especially the lower predictability when using SLP anomalies than teleconnection indices in spring. Reducing the number of predictors (smaller domains of SLP anomalies) or increasing the sample size (longer time interval) for Ridge Regression training could improve the predictive skill of SLP anomalies. Therefore, in the next subsections, we conduct the spatial and temporal sensitivity study of the global C-cycle to SLP anomalies.

### 3.2 Sensitivity to the SLP domains

325 Here, we test the sensitivity of the global C-cycle IAV predictability by using different spatial domains of SLP as predictors in Ridge Regression. The SLP domains are selected over different latitudinal bands in DJF and MAM separately (Fig. 4). We find improved predictability in both seasons when selecting smaller spatial domains (particularly including the tropics to high latitudes of the Southern Hemisphere) rather than global SLP anomalies. MAM fields show lower predictability in general and are less sensitive to the spatial domain considered. In the following, we show the results for DJF, the results for MAM can be found in Appendix A Fig. A7. Here we only show the results of the period 1980–2017. The results of the period 1959–2017 show a similar trend (see Appendix A Fig. A6).

Consistent with previous studies (Zeng et al., 2005; Piao et al., 2020), the tropical domain corresponds to higher predictability for all datasets, but stronger predictability are found for regions extending from the tropics to the Southern Hemisphere



(Fig. 4). Including Northern Hemisphere regions results in lower predictability. The domain 18° N–72° S shows the highest  
335 predictability, with  $\rho_{\text{SLP}}$  of 0.81 for  $AGR_R$  and 0.85 for  $SL_{\text{Resid}}$  in 1980–2017.

The results for net atmosphere-land fluxes estimated by atmospheric inversions are consistent with those of  $AGR_R$ , with  $\rho_{\text{SLP}}$  of 0.70 for  $SL_{\text{CAM5}}$  and 0.76 for  $SL_{\text{CarboScope}}$  in the same domain of 18° N–72° S. The values of  $\rho_{\text{SLP}}$  of  $SL_{\text{DGVMs}}$  are systematically lower than the other datasets, independently of the domain.

The weaker values of predictability when extending SLP domains from tropics to Northern Hemisphere (Fig. 4) might be due  
340 to the local rather than global impacts of large-scale atmospheric circulation variability in Northern Hemisphere to land sink IAV. Additional explanations include the fact that carbon fluxes are weaker in winter Northern Hemisphere, so that large-scale atmospheric circulation variability exerts weaker influence in the global land sink, and that there are strong compensatory effects of gross primary productivity versus terrestrial ecosystem respiration in the Northern Hemisphere in response to water and temperature variations (Jung et al., 2017; Wang et al., 2022).

The increasing predictability of global C-cycle IAV when using SLP fields extending from tropics to Southern Hemisphere  
(Fig. 4) is likely due to the strong contribution of semi-arid regions in the Southern Hemisphere extratropics to the global sink through their drought/wet anomalies (Poulter et al., 2014; Ahlström et al., 2015). The drought/wet anomalies in these regions are controlled by large-scale atmospheric circulation variability in the Southern Hemisphere (ENSO and ENSO related modes) and to the interactions between ENSO and other large-scale atmospheric circulation modes in the Southern Hemisphere, such  
350 as the synergistic effects from ENSO, IOD and the SAM on Australia C-cycle variability (Cleverly et al., 2016).

### 3.3 Sensitivity to the temporal domains

Because of multi-decadal variability in the climate system, it is possible that the relationships found for short intervals are not stable. In order to investigate whether these results depend on the temporal domain considered, we additionally analyze the influence of different temporal domains (30-yr interval sliding window) on the predictability of global C-cycle IAV by  
355 selecting different temporal domains, and performing the Ridge Regression separately for the global and the tropical domains (Fig. 5).

Results show stronger predictability of  $AGR_R$  confined to the tropics of SLP domains in earlier periods and an intensification of these predictability for the SLP domains extending to the Southern Hemisphere over the study period. In some periods, the tropics and Southern extratropics domain shows the highest values of  $\rho_{\text{SLP}}$ , for example in 1978–2011 and 1984–2015 (Fig. 5).  
360 There is, however, high temporal variability in the predictability and of the most relevant spatial domain, with other periods showing higher global coherence (e.g. 1968–2001). It is unclear whether these temporal variations occur randomly due to internal variability in the climate system, or are influenced by external forcing. Potential explanations for this pattern include trends found in SLP variability over the Pacific and Southern Atlantic (Schneider et al., 2012; IPCC, 2013; Roxy et al., 2019), or enhanced sensitivity of C-cycle variability to climatic drivers, particularly in semi-arid areas, under progressive climate  
365 change (Wang et al., 2014; Poulter et al., 2014).

Understanding and attributing these changes to given processes is beyond the scope of this study, but these results highlight the importance of the temporal domain when analyzing IAV in the global C-cycle. Since the observed CO<sub>2</sub> time-series are

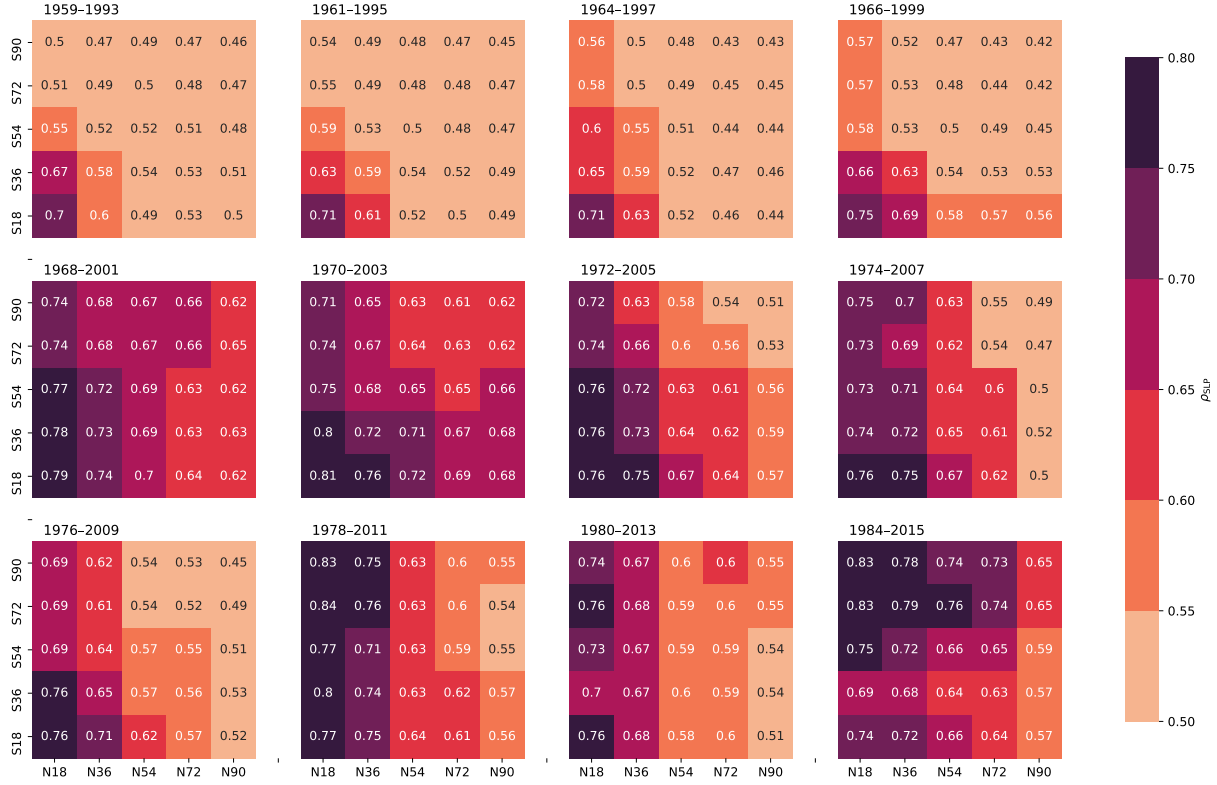
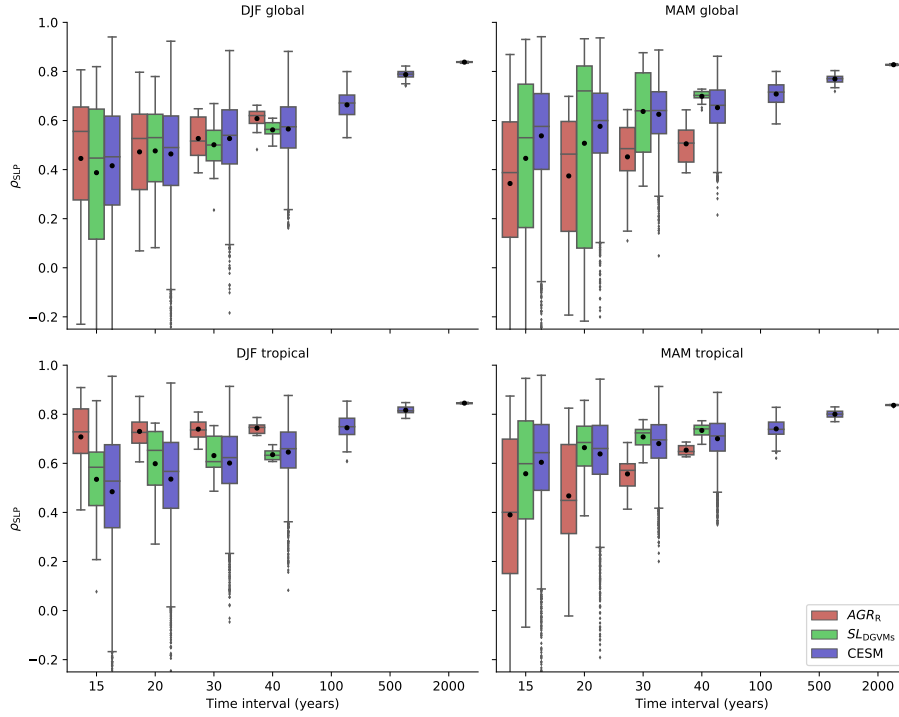


**Figure 5.** Predictability of  $AGR_R$  with DJF SLP over various latitude domains. A 30-yr sliding window in the period 1959–2017 with a one year step is created. The starting and end year of each interval is labeled on the top of each heat map. Here we only show the results of every second starting year, the full results are in Appendix A Fig. A9.

short and cover only limited temporal domains, results are likely to be affected by multi-decadal internal climate variability, in addition to external forcing. Moreover, the data-driven Ridge Regression method to quantify circulation-induced global C-cycle variability uses a large number of predictors, while only relatively short time series are available for training, which may negatively affect the model's performance. Therefore, we further test the sensitivity of the predictability to the length of the time-series (Fig. 6). We test the predictability of global C-cycle IAV for different lengths of the temporal domain: 15, 20, 30 and 40 years for the datasets in Global Carbon Budget 2018 and CESM simulations and 100, 500 and 2000 years for CESM only.

The boxplots in Fig. 6 show the distribution of predictability calculated for multiple time intervals, each time interval using a sliding window over the whole period of the respective time-series of  $AGR_R$ ,  $SL_{DGVMs}$  and CESM. The spread of predictability provides an indication of internal variability in the predictability of global C-cycle IAV due to the choice of temporal domain and the uncertainty in the Ridge Regression fit for a large number of predictors and comparatively small number of training samples.



(a)

**Figure 6.** Predictability of  $AGR_R$ ,  $SL_{DGVMs}$ , and CESM NBP under various time intervals. The predictability of  $AGR_R$  and  $SL_{DGVMs}$  are both within the period 1959–2017, with a 1 year step sliding window of 15, 20, 30, and 40 year. The predictability of CESM in the period 1000–5000 and covers extra intervals of 100, 500, 2000 years. The distribution of the predictability under each sliding window with SLP in DJF global, MAM global, DJF tropical and MAM tropical. Tropical domains are  $18^\circ$  N– $18^\circ$  S for SLP as predictors in predicting  $AGR_R$  and  $SL_{DGVMs}$ , and  $20^\circ$  N– $20^\circ$  S for SLP as predictors in predicting CESM. Note that the mean values are in black dots.

380 We find that the longer the time interval the higher the mean predictability and the smaller the variation, i.e. the less dependent are the results on the temporal domain considered (Fig. 6). However, the mean value tends to be lower than the median for intervals shorter than 30 years, and similar to the median for longer intervals. The lower mean is influenced by some domains with very low or even negative predictability from invalid predictions in shorter time intervals.

The mean predictability of  $AGR_R$  in winter for the global domain increases from 0.45 to 0.61 from 15–yr to 40–yr re-  
 385 spectively, while the spread (maximum  $\rho_{SLP}$  - minimum  $\rho_{SLP}$ ) decreases from 1.04 to 0.18. Predictability for  $SL_{DGVMs}$  are consistent with those of  $AGR_R$ , with systematically lower mean predictability for DJF and higher for spring, but similar spread in both. The mean value of predictability for CESM in SLP DJF over the global domain increases from 0.42 (15–yr) to 0.57 (40–yr) and to 0.84 (2000–yr), and the spread decreases from 1.72 to 0.72 and to 0.008, respectively.

At global scale, the predictive skill of SLP anomalies with  $AGR_R$  and with models from  $SL_{DGVMs}$  and CESM are different in winter and spring (Fig. 6). Predictability of  $AGR_R$  is higher with winter SLP ( $\rho_{SLP}$  is 0.61 in 40-yr DJF), but predictability of  $SL_{DGVMs}$  and CESM are higher with spring SLP ( $\rho_{SLP}$  in 40-yr MAM is 0.70 and 0.65, respectively).

When limiting the SLP domain to the tropics, results follow the same patterns as those at the global scale, but with better predictive skill:  $AGR_R$  shows the highest mean predictability of 0.74 for intervals of 40 years in winter (Fig. 6).  $SL_{DGVMs}$  shows the highest mean predictability, with  $\rho_{SLP}$  of 0.73 for 40-yr spring (Fig. 6), a result that is very similar to those of CESM for the same temporal length ( $\rho_{SLP} = 0.70$ ). We find that with different time intervals, tropical SLP in winter leads to higher predictability of  $AGR_R$  than global SLP fields. While the spring tropical SLP only shows slightly higher predictive skill than global SLP for  $SL_{DGVMs}$  and CESM.  $AGR_R$  is highly influenced by winter tropical SLP, while  $SL_{DGVMs}$  and CESM are more sensitive to spring tropical SLP (Fig. 6). This is consistent with the results of Fig. 4 even when different time intervals are considered. This might be due to that Earth System Models, as CESM used here, have been found to not reliably simulate the seasonal timing of ENSO occurrence (Sheffield et al., 2013). The predictive skill of SLP in seasonal and domain differences between observation-based data and models ( $SL_{DGVMs}$  and CESM) could be used as an indicator to reveal their different driving mechanisms.

We evaluate the error rate of valid predictions within each time interval sliding window in Fig. 6 (i.e., the fraction of predictions in one time interval sliding window with  $\rho_{SLP}$  of significance  $P > 0.05$ ) for  $AGR_R$ ,  $SL_{DGVMs}$ , and CESM (see Appendix A Fig. A10). We find that at least 30-year long intervals are needed for robust prediction of global C-cycle IAV. For periods shorter than 30 years, the rate of invalid predictions (in the sense given above) can be higher than 40 % for most datasets and SLP domains and seasons. It is worth noting that even when predicting  $AGR_R$  by using winter SLP in the tropical domain, the error rate can still be as low as 13% in 15-yr interval. From the 15-yr to 30-yr interval, the error rate of  $AGR_R$  reduces from 0.4 to 0 in winter global and 0.13 to 0 in winter tropical. The error rate decreases to less than 0.16 in 30-yr interval, except  $AGR_R$  decreases to 0.24 in spring global, which also matches the relative low predictability of spring SLP anomalies in the period 1980–2017 with different spatial domains (see Appendix A Fig. A7 b). All error rates are reduced to almost zero in a 40-yr interval.

## 4 Conclusions

The major objective of this study is to explore the relationship between SLP anomalies (as a proxy of large-scale atmospheric circulation variability) and the global C-cycle IAV. Specifically, our goals are 1) to investigate the skill of SLP to predict global C-cycle IAV using Ridge Regression and to compare with traditional teleconnection indices, and 2) to establish statistical links at different spatio-temporal scales between large-scale atmospheric circulation variability and global C-cycle IAV.

First, we find that boreal winter and spring SLP anomalies allow predicting IAV of atmospheric  $CO_2$  growth rate and IAV of the global land sink, with correlations between predicted and reference values between 0.70–0.84 when using winter SLP fields. This is comparable or higher than the predictive skill of a similar model using 15 teleconnection indices as predictors. The spatial patterns of the Ridge Regression coefficients reveal a strong influence of large-scale atmospheric circulation

variability on global C-cycle IAV, particularly in the El Niño / Southern Oscillation and West Pacific domains. Second, the comprehensive spatio-temporal sensitivity analysis indicates an increasing sensitivity of global C-cycle IAV to large-scale atmospheric circulation variability during boreal winter in the Southern Hemisphere extratropics in the recent decades. This  
425 increased sensitivity may be influenced by internal climate variability or by enhanced sensitivity of global C-cycle variability to externally forced changes, but requires further research. Finally, we find that time-series of at least 30 years are needed for robust predictability of global C-cycle IAV. For shorter time-series, predictability is highly dependent on the particular period considered, and thus largely due to statistical artifacts of random internal climate variability in the fitting process.

Overall, Ridge Regression using seasonal SLP fields as predictors of global C-cycle variability provides a novel and efficient  
430 data-driven approach for detecting the relationship of large-scale atmospheric circulation variability to global C-cycle variability. Compared to teleconnection indices, this approach requires no pre-defined spatial configurations and is more flexible to the particular domain considered and shows equal or higher predictability of global C-cycle IAV. This method allows quantifying the contribution of atmospheric dynamical processes in driving variability in the C-cycle at global and regional scales, and may further be useful for attributing observed changes to internal climate variability versus anthropogenic climate change.



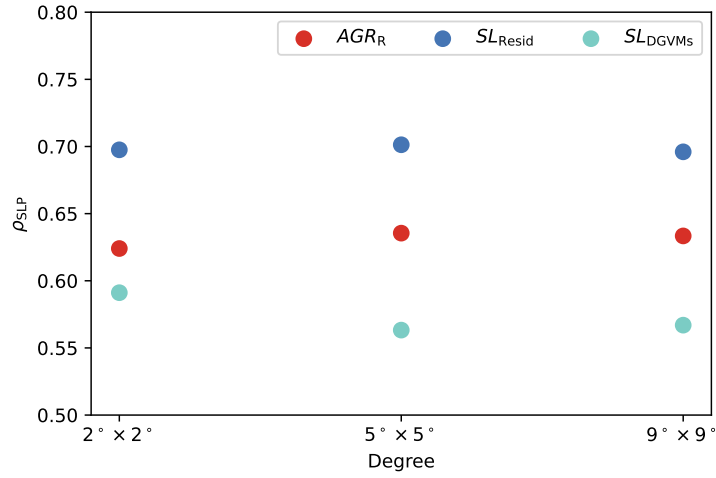


**Figure A1.**  $\rho_{SLP}$  of  $AGR_R$ ,  $SL_{Resid}$  and  $SL_{DGVMs}$  under different DJF SLP resolution ( $2^\circ \times 2^\circ$ ,  $5^\circ \times 5^\circ$ ,  $9^\circ \times 9^\circ$ ) by Ridge Regression leave-one-out cross-validation in period of 1959–2017.

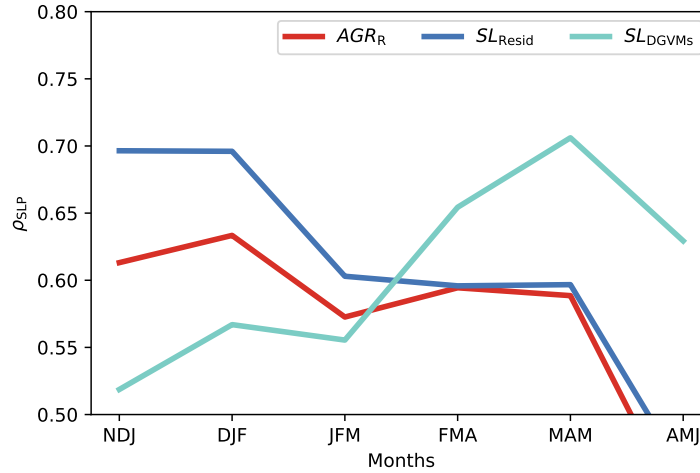


**Figure A2.**  $\rho_{SLP}$  of  $AGR_R$ ,  $SL_{Resid}$  and  $SL_{DGVMs}$  under different seasonal SLP (with different month combination) by Ridge Regression leave-one-out cross-validation in period of 1959–2017. Each combination represents: NDJ (November, December, and January), DJF (December, January, and February), JFM (January, February, and March), MAM (March, April, and May), AMJ (April, May, and June).



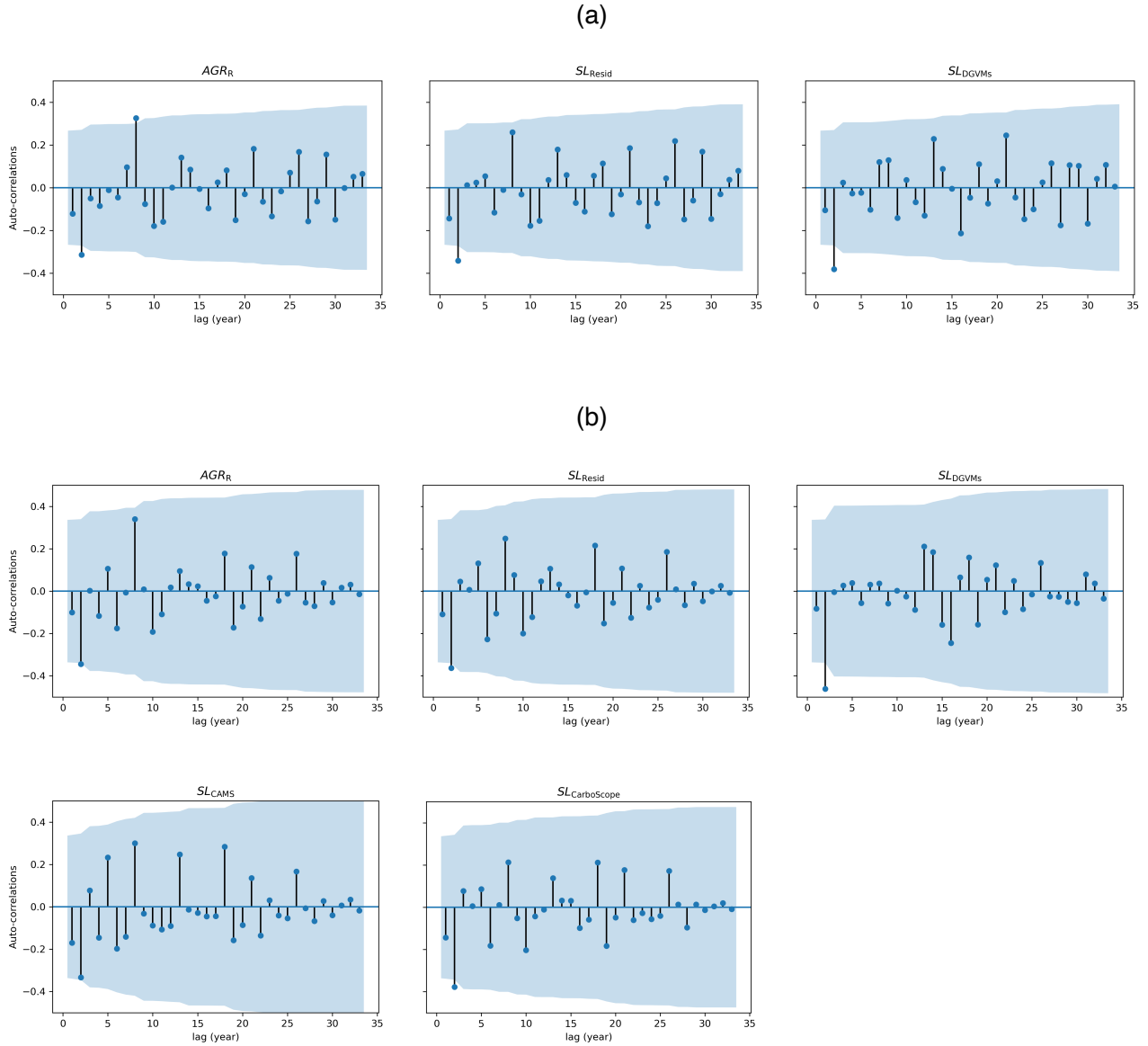


**Figure A3.** Time series auto-correlations of pre-treated CO<sub>2</sub> time-series in period (a) 1959–2017 for  $AGR_R$ ,  $SL_{Resid}$  and  $SL_{DGVMs}$ . (b) 1980–2017 included two more inversions  $SL_{CAMS}$  and  $SL_{CarboScope}$ . The shaded areas are the 95% confidence interval of the calculated auto-correlation under different lags.

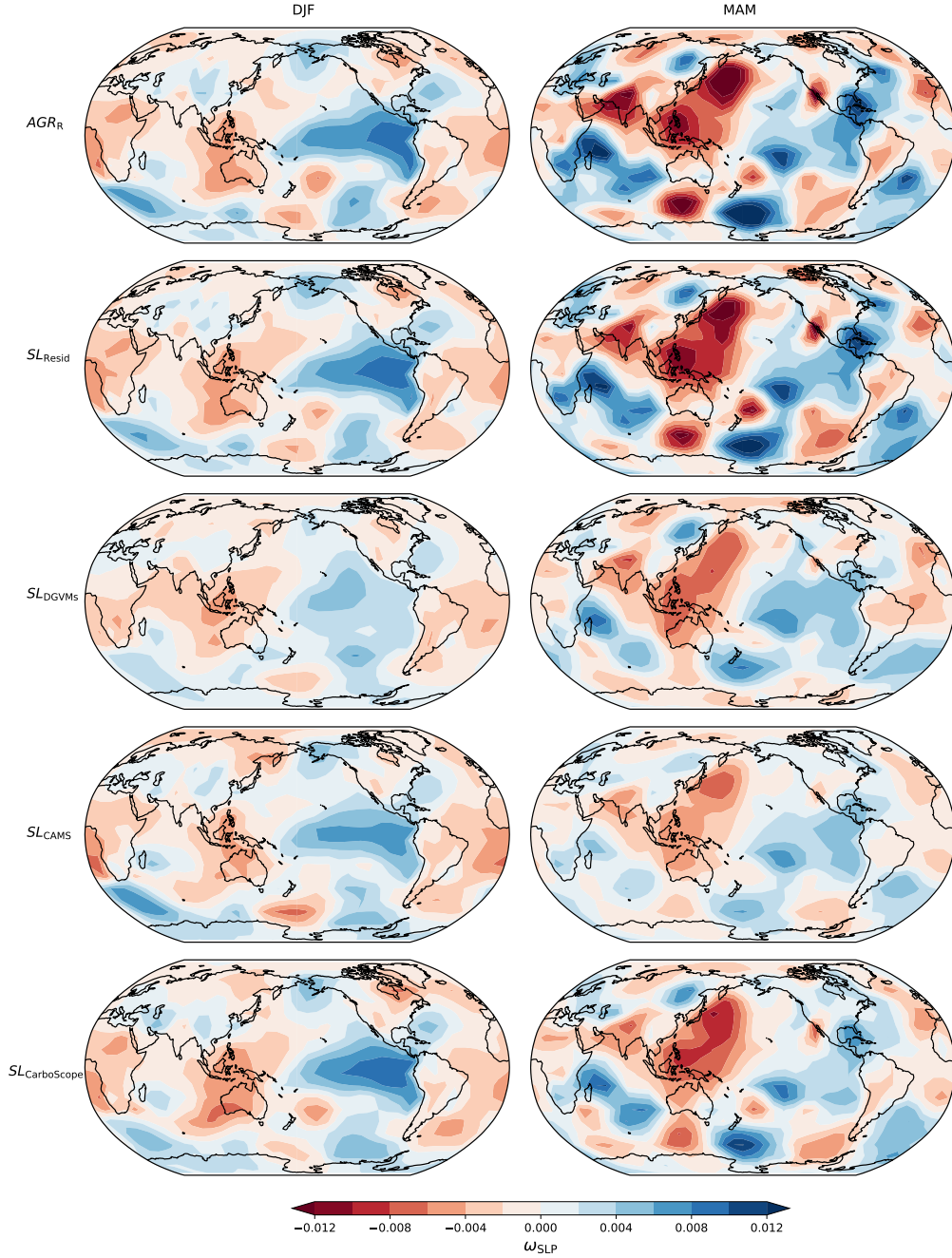


**Figure A4.** Distribution of  $\omega_{SLP}$  with the time-series of  $AGR_R$  (top row),  $SL_{Resid}$  (second row),  $SL_{DGVMs}$  (third row),  $SL_{CAMs}$  (fourth row) and  $SL_{CarboScope}$  (last row) in DJF (left column) and MAM (right column) based on SLP fields in the period 1980–2017.  $\omega_{SLP}$  are the mean of the  $n = 34$  run Ridge Regression coefficients. Note that  $\rho_{SLP}$  of  $SL_{CAMs}$  MAM has  $P > 0.5$ .

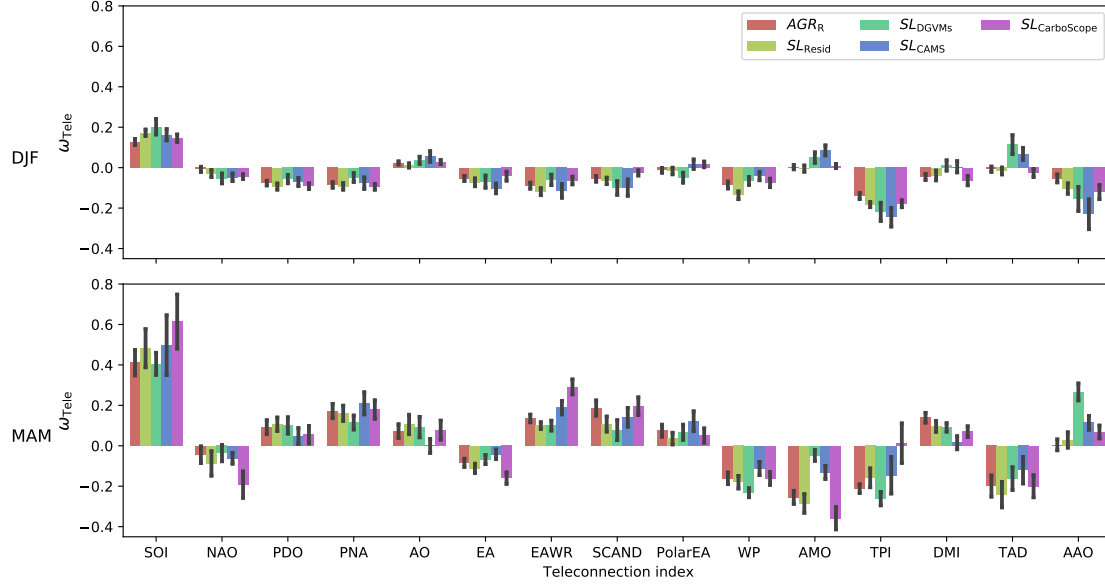


**Figure A5.** Distribution of  $\omega_{Tele}$  with the time-series of  $AGR_R$ ,  $SL_{Resid}$ ,  $SL_{DGVMs}$ ,  $SL_{CAMS}$  and  $SL_{CarboScope}$  based on teleconnection indices in period of 1980–2017.

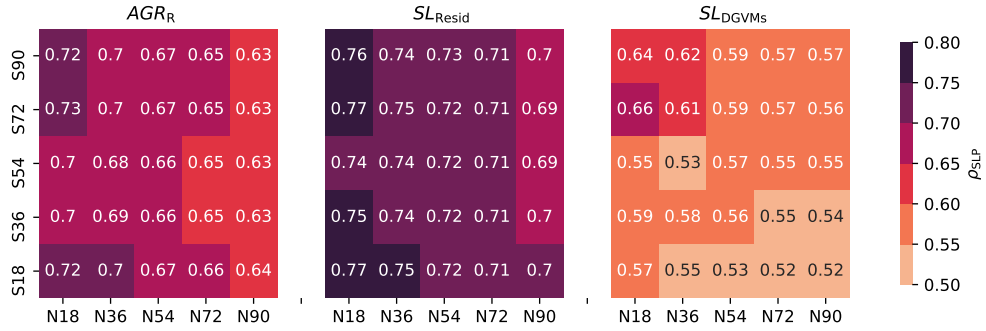


**Figure A6.** Heat map of  $\rho_{SLP}$  with  $CO_2$  time-series over various SLP latitude domains in DJF. Each heat map contains  $5 \times 5$  squares, and each square represents one domain of SLP. For example, the square  $36^\circ N$ – $72^\circ S$  is the domain of SLP extending from  $36^\circ N$  to  $72^\circ S$ . All latitudinal domains include the tropical area ( $18^\circ N$ – $18^\circ S$ ). The top right square thus represents global scale SLP.  $\rho_{SLP}$  of  $AGR_R$ ,  $SL_{Resid}$ ,  $SL_{DGVMs}$  in 1959–2017.



**Figure A7.** Heat map of  $\rho_{SLP}$  with CO<sub>2</sub> time-series over various SLP latitude domains in MAM. Each heat map contains 5×5 squares, and each square represents one specific domain of SLP. For example, the square 36° N–72° S is the domain of SLP extending from 36° N extending to 72° S. All latitudinal domains include the tropical area (18° N–18° S). The top right square thus represents global scale SLP. Time series is from (a) 1959–2017 for *AGR<sub>R</sub>*, *SL<sub>Resid</sub>* and *SL<sub>DGVMs</sub>*. (b) 1980–2017 included two more inversions *SL<sub>CAMS</sub>* and *SL<sub>CarboScope</sub>*.

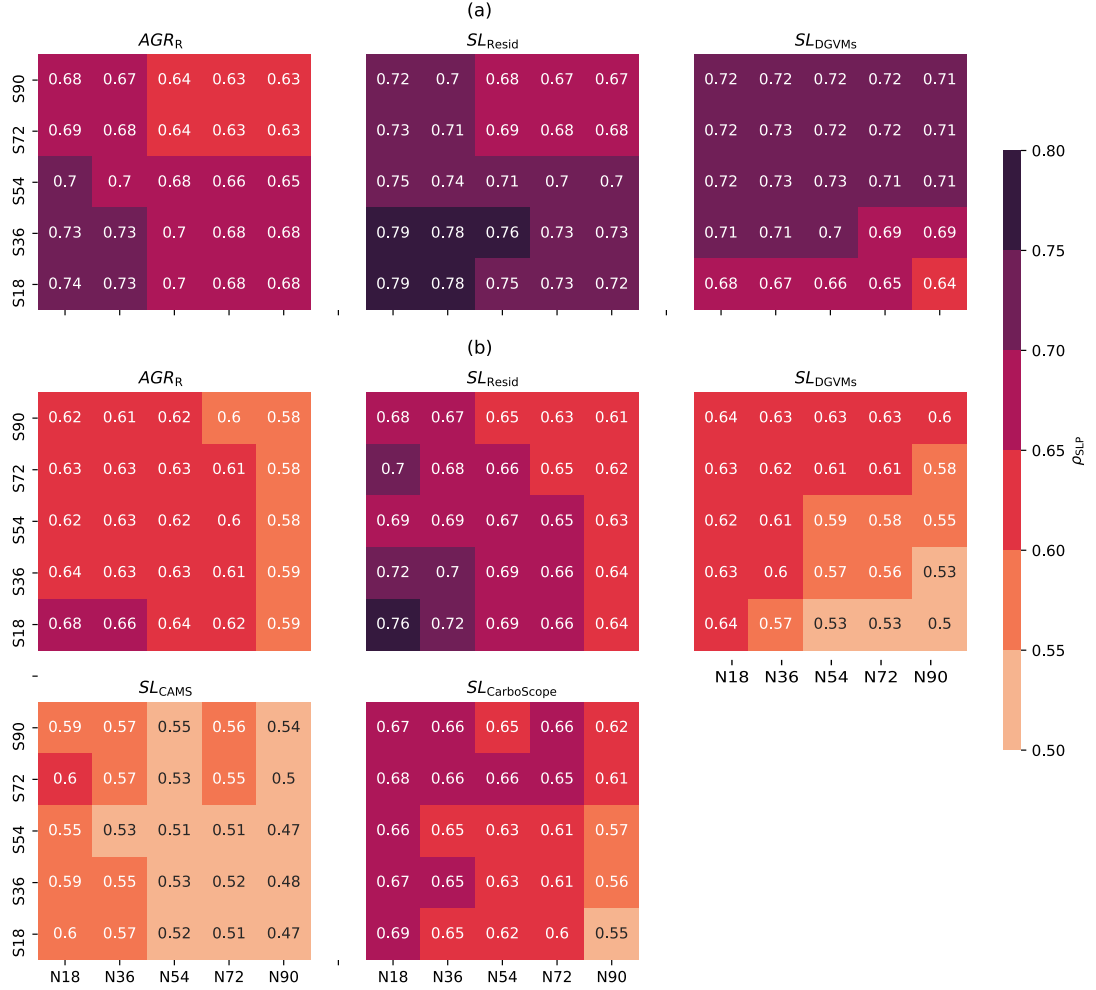


**Figure A8.** Heat map of  $\rho_{SLP}$  with CO<sub>2</sub> time-series over various SLP latitude domains in DJF+MAM. Each heat map contains 5×5 squares, and each square represents one specific domain of SLP. For example, the square 36° N–72° S is the domain of SLP extending from 36° N extending to 72° S. All latitudinal domains include the tropical area (18° N–18° S). The top right square thus represents global scale SLP. Time series is from (a) 1959–2017 for *AGR<sub>R</sub>*, *SL<sub>Resid</sub>* and *SL<sub>DGVMs</sub>*. (b) 1980–2017 included two more inversions *SL<sub>CAMS</sub>* and *SL<sub>CarboScope</sub>*.

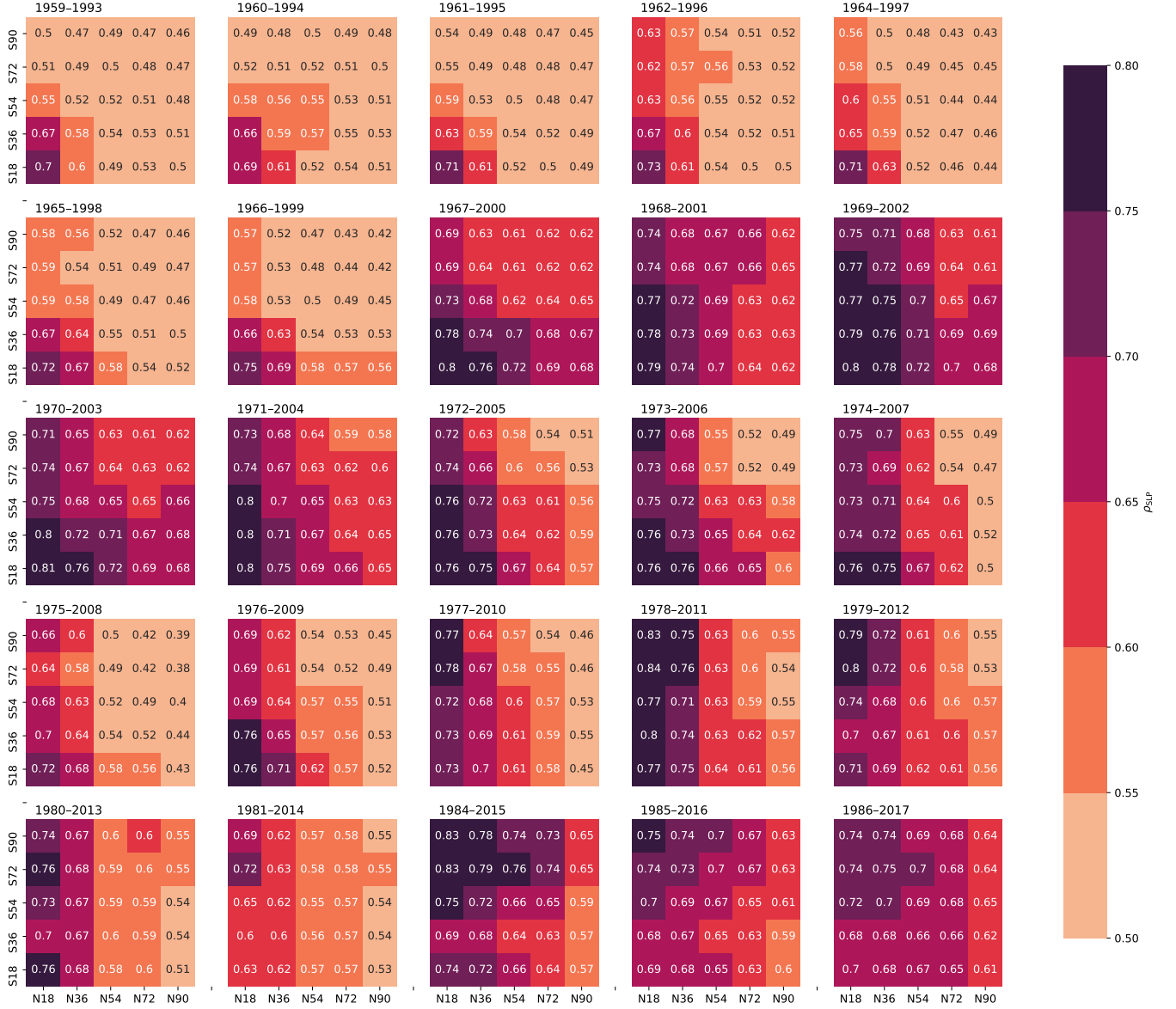


**Figure A9.** Heat map of  $\rho_{\text{SLP}}$  of  $AGR_R$  with DJF SLP over various latitude domains. A 30-yr sliding window in the period of 1959–2017 with a one year step is created. The starting and end year of each interval is labeled on the top of each heat map.

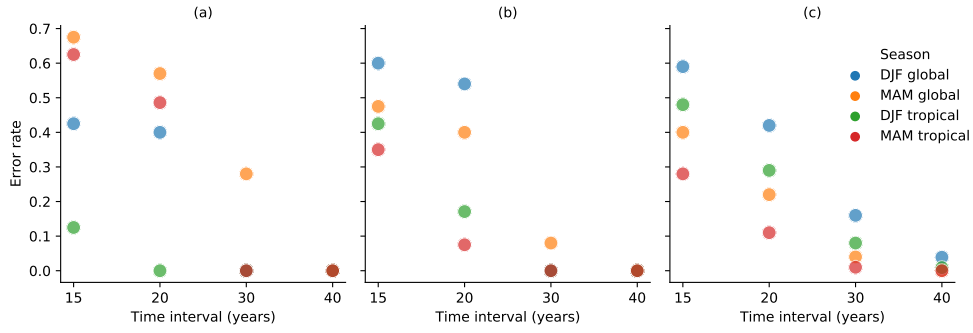


**Figure A10.** Error rate of the sliding window in 15, 20, 30 and 40 year intervals. For each sliding window, the error rate is calculated by the number of invalid predictions (with significance  $P > 0.05$  in  $\rho_{SLP}$  of  $CO_2$  time-series) divided by the number of total predictions. With SLP in DJF global, MAM global, DJF tropical and MAM tropical as predictors, the error rate of  $\rho_{SLP}$  of (a)  $AGR_R$ , (b)  $SL_{DGVMs}$ , and (c) CESM are plotted.



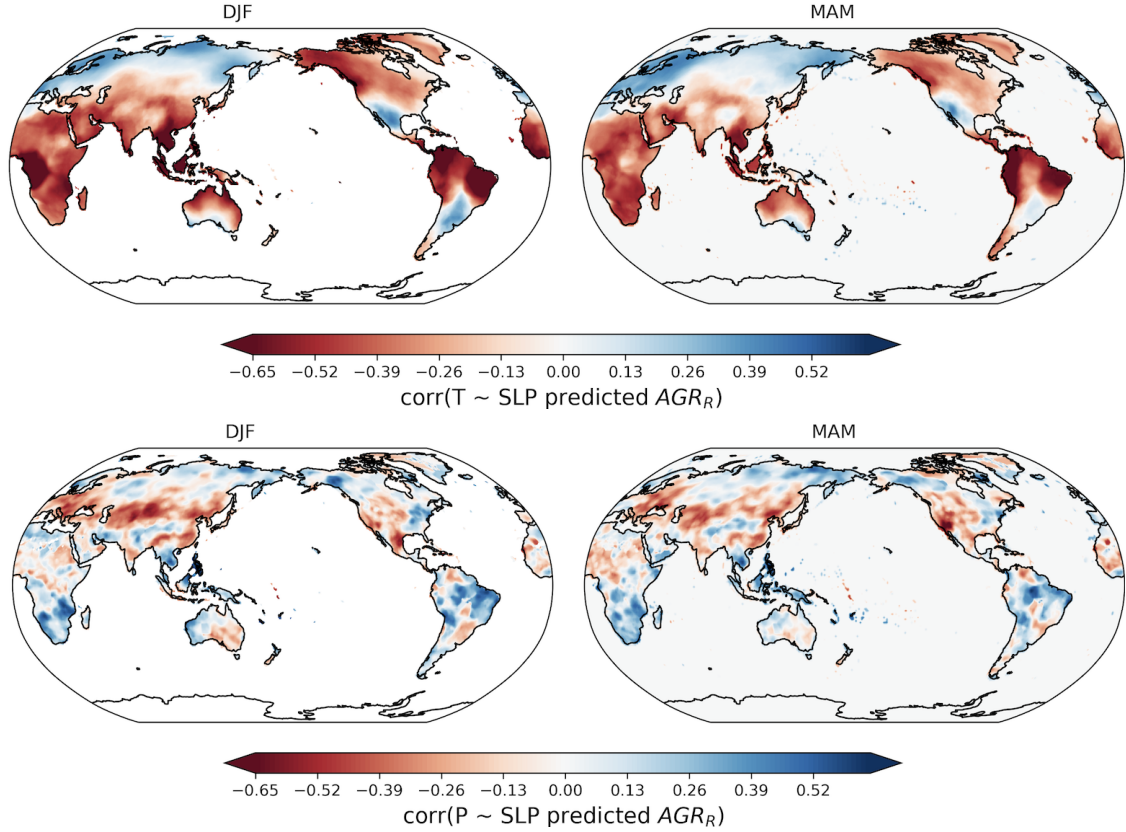


**Figure A11.** The spatial distribution of Pearson correlations between global SLP predicted  $AGR_R$  (one time-series) to global pixel-based land temperature/precipitation anomalies (both from CRU TS4.05 (Harris et al., 2020) monthly dataset, aggregated to annual mean temperature/annual sum precipitation, and detrended by LOWESS), in the period 1980–2017. The top panel shows the spatial distribution of Pearson correlations between pixel-based land temperature anomalies to global SLP predicted  $AGR_R$  for DJF (left) and MAM (right), and the bottom panel shows Pearson correlations of land precipitation anomalies.

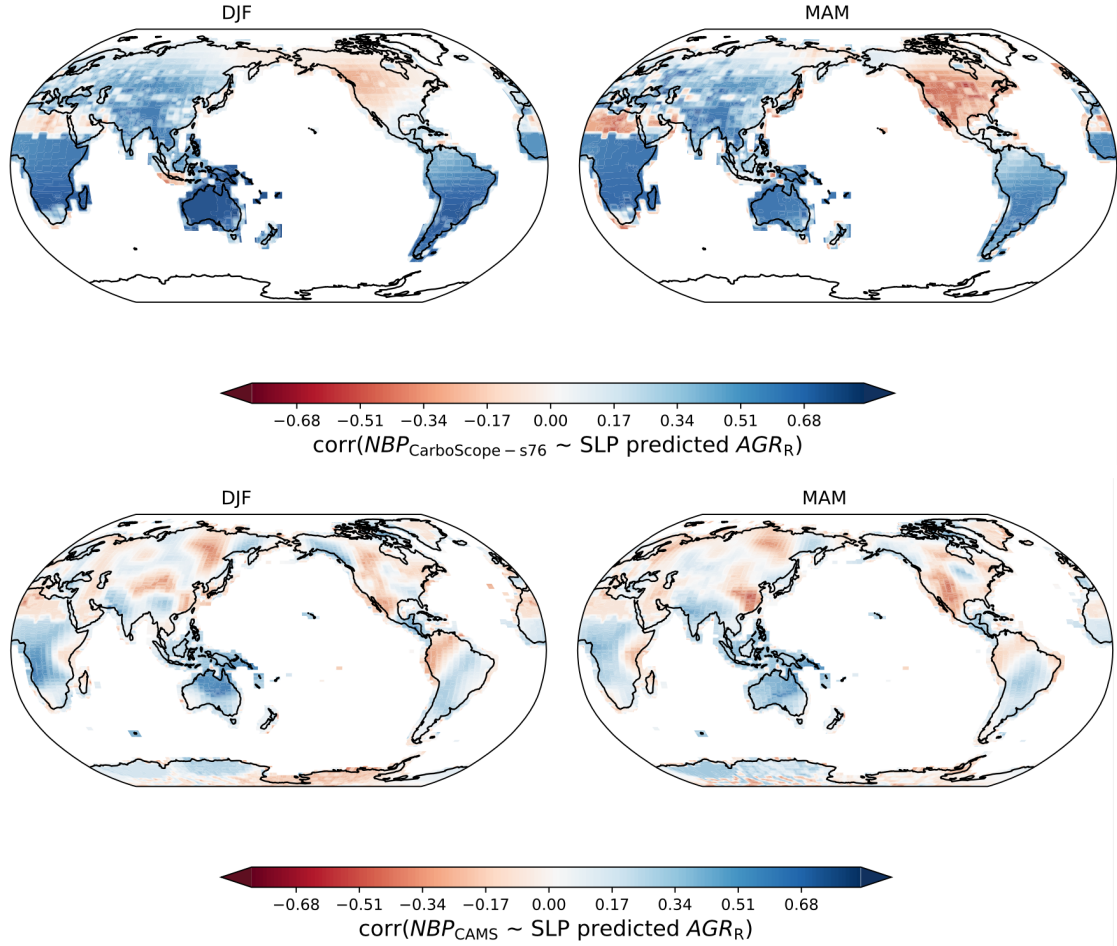


**Figure A12.** The spatial distribution of Pearson correlations between global DJF/MAM SLP predicted  $AGR_R$  (one time-series) with pixel-based annual sum NBP variation (LOWESS detrended) from atmospheric inversion CarboScope s76 (Bastos et al., 2020; Chevallier et al., 2005; Rödenbeck et al., 2003) (upper panel) and CAMS (Bastos et al., 2020; Chevallier et al., 2005; Rödenbeck et al., 2003) (lower panel), in the period 1980–2017.

## Appendix B: Data availability

The Global Carbon Budget 2018 dataset (Le Quéré et al. (2018)) is available at <https://www.icos-cp.eu/science-and-impact/global-carbon-budget/2018>. The two atmospheric inversion datasets are available in Bastos et al. (2019). The monthly sea level pressure is from ERA5 reanalysis available at Climate data store, for the period 1959-1978 is from Bell et al. (2020) and the  
440 period 1979-2017 is from Hersbach et al. (2019). The download links for the 15 teleconnection indices are available in Table 1 of Section 2.1.2, last access on August 2021. The sea level pressure and NBP from CESM1.2 is available in Stolpe et al. (2019).

## Appendix C: Code availability

The Python scripts are available at <https://edmond.mpdl.mpg.de/privateurl.xhtml?token=8f717b4f-aea2-4a9b-96a3-efc8487e54af>

### *Author contributions.*

445 NL processed the data, performed the analysis and wrote the first draft of the manuscript. SS, AB, MR designed the study. SS pre-processed the CESM1.2 data. All authors contributed to design the methodology and to the writing of the manuscript.

### *Competing interests.*

The authors declare that they have no conflict of interest.

### *Disclaimer.*

450 Publisher's note: Copernicus Publications remains neutral with regard to jurisdictional claims in published maps and institutional affiliations.

*Acknowledgements.* Markus Reichstein and Alexander J. Winkler acknowledge support by the European Research Council (ERC) Synergy Grant "Understanding and Modelling the Earth System with Machine Learning (USMILE)" under the Horizon 2020 research and innovation programme (Grant agreement No. 855187).



## References

- Ahlström, A., Raupach, M. R., Schurgers, G., Smith, B., Arneth, A., Jung, M., Reichstein, M., Canadell, J. G., Friedlingstein, P., Jain, A. K., Kato, E., Poulter, B., Sitch, S., Stocker, B. D., Viovy, N., Wang, Y. P., Wiltshire, A., Zaehle, S., and Zeng, N.: The dominant role of semi-arid ecosystems in the trend and variability of the land CO<sub>2</sub> sink, *Science*, 348, 895–899, <https://doi.org/10.1126/science.aaa1668>, 2015.
- Bacastow, R. B.: Modulation of atmospheric carbon dioxide by the Southern Oscillation, *Nature*, 261, 116–118, <https://doi.org/10.1038/261116a0>, 1976.
- Ballantyne, A. P., Alden, C. B., Miller, J. B., Tans, P. P., and White, J. W. C.: Increase in observed net carbon dioxide uptake by land and oceans during the past 50 years, *Nature*, 488, 70–72, <https://doi.org/10.1038/nature11299>, 2012.
- Barnston, A. G. and Livezey, R. E.: Classification, seasonality and persistence of low-frequency atmospheric circulation patterns, *Monthly Weather Review*, 115(6), 1083–1126, [https://doi.org/10.1175/1520-0493\(1987\)115<1083:CSAPOL>2.0.CO;2](https://doi.org/10.1175/1520-0493(1987)115<1083:CSAPOL>2.0.CO;2), 1987.
- Basile, S. J., Lin, X., Wieder, W. R., Hartman, M. D., and Keppel-Aleks, G.: Leveraging the signature of heterotrophic respiration on atmospheric CO<sub>2</sub> for model benchmarking, *Biogeosciences*, 17, 1293–1308, <https://doi.org/10.5194/bg-17-1293-2020>, 2020.
- Bastos, A., Running, S. W., Gouveia, C., and Trigo, R. M.: The global NPP dependence on ENSO: La Niña and the extraordinary year of 2011, *JGR Biogeosciences*, 118, 1247–1255, <https://doi.org/10.1002/jgrg.20100>, 2013.
- Bastos, A., Friedlingstein, P., Sitch, S., Chen, C., Mialon, A., Wigneron, J.-P., Arora, V. K., Briggs, P. R., Canadell, J. G., Ciais, P., Chevallier, F., Cheng, L., Delire, C., Haverd, V., Jain, A. K., Joos, F., Kato, E., Lienert, S., Lombardozzi, D., Melton, J. R., Myneni, R., Nabel, J. E. M. S., Pongratz, J., Poulter, B., Rödenbeck, C., Séférian, R., Tian, H., van Eck, C., Viovy, N., Vuichard, N., Walker, A. P., Wiltshire, A., Yang, J., Zaehle, S., Zeng, N., and Zhu, D.: Impact of the 2015/2016 El Niño on the terrestrial carbon cycle constrained by bottom-up and top-down approaches, *Philosophical Transactions of the Royal Society B: Biological Sciences*, 373(1760), 20170 304, <https://doi.org/10.1098/rstb.2017.0304>, PMID: 20808728; PMCID: PMC2929880., 2018.
- Bastos, A., Sullivan, M., Ciais, P., Makowski, D., Sitch, S., Friedlingstein, P., Chevallier, F., Rödenbeck, C., Pongratz, J., Luijkx, I., Patra, P., Peylin, P., Canadell, J., Lauerwald, R., Li, W., Smith, N., Peters, W., Goll, D., Jain, A., Kato, E., Lienert, S., Lombardozzi, D., Haverd, V., Nabel, J., Tian, H., Walker, A., and Zaehle, S.: Aggregated regional estimates of net atmosphere-land CO<sub>2</sub> fluxes from the five atmospheric inversions and 16 Dynamic Global Vegetation Models, supplemental data to Bastos et al, 2019 (<https://doi.org/10.1029/2019GB006393>), <https://doi.org/10.18160/1SVH-3DNB>, 2019.
- Bastos, A., O’Sullivan, M., Ciais, P., Makowski, D., Sitch, S., Friedlingstein, P., Chevallier, F., Rödenbeck, C., Pongratz, J., Luijkx, I. T., Patra, P. K., Peylin, P., Canadell, J. G., Lauerwald, R., Li, W., Smith, N. E., Peters, W., Goll, D. S., Jain, A., Kato, E., Lienert, S., Lombardozzi, D. L., Haverd, V., Nabel, J. E. M. S., Poulter, B., Tian, H., Walker, A. P., and Zaehle, S.: Sources of uncertainty in regional and global terrestrial CO<sub>2</sub> exchange estimates, *Global Biogeochemical Cycles*, 34(2), <https://doi.org/10.1029/2019GB006393>, 2020.
- Bell, B., Hersbach, H., Berrisford, P., Dahlgren, P., Horányi, A., Muñoz Sabater, J., Nicolas, J., Radu, R., Schepers, D., Simmons, A., Soci, C., and Thépaut, J.-N.: ERA5 monthly averaged data on pressure levels from 1950 to 1978 (preliminary version), Copernicus Climate Change Service (C3S) Climate Data Store (CDS), <https://cds.climate.copernicus.eu/cdsapp#!dataset/reanalysis-era5-pressure-levels-monthly-means-preliminary-back-extension?tab=overview>, last accessed on December 17, 2020, 2020.

- Boden, T. A., Marland, G., and Andres, R. J.: Global, Regional, and National Fossil-Fuel CO<sub>2</sub> Emissions, Tech. rep., Oak Ridge National Laboratory, U.S. Department of Energy, Oak Ridge, Tenn., USA, [http://cdiac.ornl.gov/trends/emis/overview\\_2014.html](http://cdiac.ornl.gov/trends/emis/overview_2014.html), last access on July 2017, 2017.
- 495 Bonan, G. B.: Ecological climatology, concepts and applications, Cambridge University press, 2016.
- Chen, W. Y. and Van den Dool, H.: Sensitivity of Teleconnection Patterns to the Sign of Their Primary Action Center, *Monthly Weather Review*, 131(11), 2885–2899, [https://doi.org/10.1175/1520-0493\(2003\)131<2885:SOTPTT>2.0.CO;2](https://doi.org/10.1175/1520-0493(2003)131<2885:SOTPTT>2.0.CO;2), 2003.
- Chevallier, F., Fisher, M., Peylin, P., Serrar, S., Bousquet, P., Bréon, F.-M., Chédin, A., and Ciais, P.: Inferring CO<sub>2</sub> sources and sinks from satellite observations: Method and application to TOVS data, *J. Geophys. Res.*, 110, D24 309, <https://doi.org/10.1029/2005JD006390>,  
500 2005.
- Ciais, P., Sabine, C., Bala, G., Bopp, L., Brovkin, V., Canadell, J., Chhabra, A., DeFries, R., Galloway, J., Heimann, M., Jones, C., Le Quéré, C., Myneni, B. R., Piao, S., and Thornton, P.: Carbon and Other Biogeochemical Cycles. In: *Climate Change 2013: The Physical Science Basis. Contribution of Working Group I to the Fifth Assessment Report of the Intergovernmental Panel on Climate Change.*, Cambridge University Press, Cambridge, United Kingdom and New York, NY, USA, [https://www.ipcc.ch/site/assets/uploads/2018/02/WG1AR5\\_all\\_final.pdf](https://www.ipcc.ch/site/assets/uploads/2018/02/WG1AR5_all_final.pdf), 2013.  
505
- Cleveland, W., Grosse, E., and Shyu, W.: Local regression models. *Statistical Models in S*, Chapman Hall, 309–376, 1991.
- Cleverly, J., Eamus, D., Luo, Q., Coupe, N. R., Kljun, N., Ma, X., Ewenz, C., Li, L., Yu, Q., and Huete, A.: The importance of interacting climate modes on Australia’s contribution to global carbon cycle extremes, *Scientific Reports*, 6, <https://doi.org/10.1038/srep23113>, 2016.
- 510 Cox, P. M., Pearson, D., Booth, B. B., Friedlingstein, P., Huntingford, C., Jones, C. D., and Luke, C. M.: Sensitivity of tropical carbon to climate change constrained by carbon dioxide variability, *Nature*, 494, 341–344, <https://doi.org/10.1038/nature11882>, 2013.
- CPC, N.: NOAA/ National Weather Service NOAA Center for Weather and Climate Prediction, Climate Prediction Center, <https://www.cpc.ncep.noaa.gov/data/teledoc/teleindcalc.shtml>, last accessed on August 11, 2021, 2008.
- Deser, C., Phillips, A., Bourdette, V., and Teng, H.: Uncertainty in climate change projections: the role of internal variability, *Clim Dyn*,  
515 38, 527–546, <https://doi.org/10.1007/s00382-010-0977-x>, 2012.
- Deser, C., Lehner, F., Rodgers, K. B., Ault, T., Delworth, T. L., DiNezio, P. N., Fiore, A., Frankignoul, C., Fyfe, J. C., Horton, D. E., Kay, J. E., Knutti, R., Lovenduski, N. S., Marotzke, J., McKinnon, K. A., Minobe, S., Randerson, J., Screen, J. A., Simpson, I. R., and Ting, M.: Insights from Earth system model initial-condition large ensembles and future prospects, *Nat. Clim. Change*, 10, 277–286, <https://doi.org/10.1038/s41558-020-0731-2>, 2020.
- 520 DeVries, T., Holzer, M., and Primeau, F.: Recent increase in oceanic carbon uptake driven by weaker upper-ocean overturning, *Nature*, 542, 215–218, <https://doi.org/10.1038/nature21068>, 2017.
- Dlugokencky, E. and Tans, P.: Trends in atmospheric carbon dioxide, National Oceanic Atmospheric Administration, Earth System Research Laboratory (NOAA/ESRL), <http://www.esrl.noaa.gov/gmd/ccgg/trends/global.html>, last access: 4 September 2018, 2018.
- Dlugokencky, E. and Tans, P.: Trends in atmospheric carbon dioxide, National Oceanic Atmospheric Administration, Earth Syem Research Laboratory (NOAA/ESRL), <http://www.esrl.noaa.gov/gmd/ccgg/trends/global.html>, last access on 3 November 2019, 2019.  
525
- Dufour, C. O., Le Sommer, J., Gehlen, M., Orr, J. C., Molines, J. M., Simeon, J., and Barnier, B.: Eddy compensation and controls of the enhanced sea-to-air CO<sub>2</sub> flux during positive phases of the Southern Annular Mode, *Global Biogeochem. Cy.*, 27, 950–961, <https://doi.org/10.1002/gbc.20090>, 2013.

Enfield, D. B., Mestas-Núñez, A. M., Mayer, D. A., and Cid-Serrano, L.: How ubiquitous is the dipole relationship in tropical Atlantic sea surface temperatures?, *Journal of Geophysical Research*, 104, 7841–7848, <https://doi.org/10.1029/1998JC900109>, 1999.

Enfield, D. B., Mestas-Núñez, A. M., and Trimble, P. J.: The Atlantic Multidecadal Oscillation and its relation to rainfall and river flows in the continental U.S., *Geophysical Research Letters*, 28(10), 2077–2080, <https://doi.org/10.1029/2000GL012745>, 2001.

Friedlingstein, P., Meinshausen, M., Arora, V. K., Jones, C. D., Anav, A., Liddicoat, S. K., and Knutti, R.: Uncertainties in CMIP5 climate projections due to carbon cycle feedbacks, *Journal of Climate*, 27(2), 511–526, <https://doi.org/10.1175/JCLI-D-12-00579.1>, 2014.

535 Friedlingstein, P., Jones, M. W., O’Sullivan, M., Andrew, R. M., Hauck, J., Peters, G. P., Peters, W., Pongratz, J., Sitch, S., Le Quéré, C., Bakker, D. C. E., Canadell, J. G., Ciais, P., Jackson, R. B., Anthoni, P., Barbero, L., Bastos, A., Bastrikov, V., Becker, M., Bopp, L., Buitenhuis, E., Chandra, N., Chevallier, F., Chini, L. P., Currie, K. I., Feely, R. A., Gehlen, M., Gilfillan, D., Gkritzalis, T., Goll, D. S., Gruber, N., Gutekunst, S., Harris, I., Haverd, V., Houghton, R. A., Hurtt, G., Ilyina, T., Jain, A. K., Joetzjer, E., Kaplan, J. O., Kato, E., Klein Goldewijk, K., Korsbakken, J. I., Landschützer, P., Lauvset, S. K., Lefèvre, N., Lenton, A., Lienert, S., Lombardozzi, D.,

540 Marland, G., McGuire, P. C., Melton, J. R., Metzl, N., Munro, D. R., Nabel, J. E. M. S., Nakaoka, S.-I., Neill, C., Omar, A. M., Ono, T., Peregón, A., Pierrot, D., Poulter, B., Rehder, G., Resplandy, L., Robertson, E., Rödenbeck, C., Séférian, R., Schwinger, J., Smith, N., Tans, P. P., Tian, H., Tilbrook, B., Tubiello, F. N., van der Werf, G. R., Wiltshire, A. J., and Zaehle, S.: Global Carbon Budget 2019, *Earth System Science Data*, 11, 1783–1838, <https://doi.org/10.5194/essd-11-1783-2019>, 2019.

Friedlingstein, P., Jones, M. W., O’Sullivan, M., Andrew, R. M., Bakker, D. C. E., Hauck, J., Le Quéré, C., Peters, G. P., Peters, W.,

545 Pongratz, J., Sitch, S., Canadell, J. G., Ciais, P., Jackson, R. B., Alin, S. R., Anthoni, P., Bates, N. R., Becker, M., Bellouin, N., Bopp, L., Chau, T. T. T., Chevallier, F., Chini, L. P., Cronin, M., Currie, K. I., Decharme, B., Djeutchouang, L. M., Dou, X., Evans, W., Feely, R. A., Feng, L., Gasser, T., Gilfillan, D., Gkritzalis, T., Grassi, G., Gregor, L., Gruber, N., Gürses, O., Harris, I., Houghton, R. A., Hurtt, G. C., Iida, Y., Ilyina, T., Luijkx, I. T., Jain, A., Jones, S. D., Kato, E., Kennedy, D., Klein Goldewijk, K., Knauer, J., Korsbakken, J. I., Körtzinger, A., Landschützer, P., Lauvset, S. K., Lefèvre, N., Lienert, S., Liu, J., Marland, G., McGuire, P. C., Melton, J. R.,

550 Munro, D. R., Nabel, J. E. M. S., Nakaoka, S.-I., Niwa, Y., Ono, T., Pierrot, D., Poulter, B., Rehder, G., Resplandy, L., Robertson, E., Rödenbeck, C., Rosan, T. M., Schwinger, J., Schwingshackl, C., Séférian, R., Sutton, A. J., Sweeney, C., Tanhua, T., Tans, P. P., Tian, H., Tilbrook, B., Tubiello, F., van der Werf, G. R., Vuichard, N., Wada, C., Wanninkhof, R., Watson, A. J., Willis, D., Wiltshire, A. J., Yuan, W., Yue, C., Yue, X., Zaehle, S., and Zeng, J.: Global Carbon Budget 2021, *Earth System Science Data*, 14, 1917–2005, <https://doi.org/10.5194/essd-14-1917-2022>, 2022.

555 Friedman, J., Hastie, T., and Tibshirani, R.: Regularization paths for generalized linear models via coordinate descent, *J Stat Softw.*, 33(1), 1–22, <https://doi.org/10.18637/jss.v033.i01>, 2010.

Frölicher, T. L., Joos, F., Raible, C. C., and Sarmiento, J. L.: Atmospheric CO<sub>2</sub> response to volcanic eruptions: The role of ENSO, season, and variability, *Global Biogeochemical Cycles*, 27(1), 239–251, <https://doi.org/10.1002/gbc.20028>, 2013.

Ghil, M.: Natural climate variability, Volume 1, *The Earth system: physical and chemical dimensions of global environmental change*, from

560 *Encyclopedia of Global Environmental Change*, John Wiley Sons, Ltd, Chichester, <http://citeseerx.ist.psu.edu/viewdoc/download?doi=10.1.1.15.3765&rep=rep1&type=pdf>, p544-549, 2002.

Gu, G. and Adler, R. F.: Precipitation and temperature variations on the interannual time scale: Assessing the impact of ENSO and volcanic eruptions, *Journal of Climate*, 24, 2258–2270, <https://doi.org/10.1175/2010JCLI3727.1>, 2011.

Hansis, E., Davis, S. J., and Pongratz, J.: Relevance of methodological choices for accounting of land use change carbon fluxes, *Global Biogeochem. Cy.*, 29, 1230–1246, <https://doi.org/10.1002/2014GB004997>, 2015.

565 Harrington, P.: *Machine learning in action*, Manning publications, p155, 164, 167, 2012.



- Harris, I., Osborn, T. J., Jones, P., and Lister, D.: Version 4 of the CRU TS monthly high-resolution gridded multivariate climate dataset, *Scientific Data*, 7, 109, <https://doi.org/10.1038/s41597-020-0453-3>, 2020.
- Hastie, T., Tibshirani, R., and Friedman, J.: *The Elements of Statistical Learning: Data Mining, Inference, and Prediction*, Springer Series in Statistics, <https://doi.org/10.1007/b94608>, p61-67, 2009.
- Hauck, J., Zeising, M., Le Quéré, C., Gruber, N., Bakker, D. C. E., Bopp, L., Chau, T. T. T., Gürses, I., Ilyina, T., Landschützer, P., Lenton, A., Resplandy, L., Rödenbeck, C., Schwinger, J., and Séférian, R.: Consistency and challenges in the ocean carbon sink estimate for the Global Carbon Budget, *Frontiers in Marine Science*, 7, 852, <https://doi.org/10.3389/fmars.2020.571720>, 2020.
- Henley, B. J., Gergis, J., Karoly, D. J., Power, S. B., Kennedy, J., and Folland, C. K.: A Tripole Index for the Interdecadal Pacific Oscillation, *Climate Dynamics*, 45, 3077–3090, <https://doi.org/10.1007/s00382-015-2525-1>, last access on August 11, 2021, 2015.
- Hersbach, H., Bell, B., Berrisford, P., Biavati, G., Horányi, A., Muñoz Sabater, J., Nicolas, J., Peubey, C., Radu, R., Rozum, I., Schepers, D., Simmons, A., Soci, C., Dee, D., and Thépaut, J.-N.: ERA5 monthly averaged data on pressure levels from 1979 to present, Copernicus Climate Change Service (C3S) Climate Data Store (CDS), <https://doi.org/10.24381/cds.6860a573>, last accessed on December 17, 2020, 2019.
- Higgins, R. W., Leetmaa, A., Xue, Y., and Barnston, A.: Dominant factors influencing the seasonal predictability of U.S. precipitation and surface air temperature, *Journal of Climate*, 13(22), 3994–4017, [https://doi.org/10.1175/1520-0442\(2000\)013<3994:DFITSP>2.0.CO;2](https://doi.org/10.1175/1520-0442(2000)013<3994:DFITSP>2.0.CO;2), 2000.
- Higgins, R. W., Leetmaa, A., and Kousky, V. E.: Relationships between climate variability and winter temperature extremes in the United States, *Journal of Climate*, 15(13), 1555–1572, [https://doi.org/10.1175/1520-0442\(2002\)015<1555:RBCVAW>2.0.CO;2](https://doi.org/10.1175/1520-0442(2002)015<1555:RBCVAW>2.0.CO;2), 2002.
- Houghton, R. A. and Nassikas, A. A.: Global and regional fluxes of carbon from land use and land cover change 1850–2015, *Global Biogeochem. Cy.*, 31, <https://doi.org/10.1002/2016GB005546>, 2017, 2017.
- Hsieh, W. W.: Nonlinear multivariate and time series analysis by neural network methods, *Rev. Geophys.*, 42, RG1003, <https://doi.org/10.1029/2002RG000112>, 2004.
- Humphrey, V., Zscheischler, J., Ciais, P., Gudmundsson, L., Sitch, S., and Seneviratne, S. I.: Sensitivity of atmospheric CO<sub>2</sub> growth rate to observed changes in terrestrial water storage, *Nature*, 560, 628–631, <https://doi.org/10.1038/s41586-018-0424-4>, 2018.
- Humphrey, V., Berg, A., Ciais, P., Gentile, P., Jung, M., Reichstein, M., Seneviratne, S. I., and Frankenberg, C.: Soil moisture–atmosphere feedback dominates land carbon uptake variability, *Nature*, 592, 65–69, <https://doi.org/10.1038/s41586-021-03325-5>, 2021.
- Hurrell, J. W., Holland, M. M., Gent, P. R., Ghan, S., Kay, J. E., Kushner, P. J., Lamarque, J.-F., Large, W. G., Lawrence, D., Lindsay, K., Lipscomb, W. H., Long, M. C., Mahowald, N., Marsh, D. R., Neale, R. B., Rasch, P., Vavrus, S., Vertenstein, M., Bader, D., Collins, W. D., Hack, J. J., Kiehl, J., and Marshall, S.: The community earth system model: a framework for collaborative research, *Bulletin of the American Meteorological Society*, 94, 1339–1360, <https://doi.org/10.1175/Bams-D-12-00121.1>, 2013.
- IPCC: Climate Change 2013: The Physical Science Basis. Contribution of Working Group I to the Fifth Assessment Report of the Intergovernmental Panel on Climate Change [Stocker, T. F. and Qin, D. and Plattner, G.-K. and Tignor, M. and Allen, S.K. and Boschung, J. and Nauels, A. and Xia, Y. and Bex, V. and Midgley, P.M. (eds.)], Cambridge University Press, Cambridge, United Kingdom and New York, NY, USA, [https://www.ipcc.ch/site/assets/uploads/2018/02/WG1AR5\\_all\\_final.pdf](https://www.ipcc.ch/site/assets/uploads/2018/02/WG1AR5_all_final.pdf), p.223, 232, 233, 470, 473, 489, 502, 504, 745, 749, 1535, 2013.
- Jones, P. D., Salinger, M. J., and Mullan, A. B.: Extratropical circulation indices in the Southern Hemisphere based on station data, *International Journal of Climatology*, 19, 1301–1317, [https://doi.org/10.1002/\(SICI\)1097-0088\(199910\)19:12<1301::AID-JOC425>3.0.CO;2-P](https://doi.org/10.1002/(SICI)1097-0088(199910)19:12<1301::AID-JOC425>3.0.CO;2-P), 1999.

- 605 Jung, M., Reichstein, M., Schwalm, C. R., Huntingford, C., Sitch, S., Ahlström, A., Arneth, A., Camps-Valls, G., Ciais, P., Friedlingstein, P., Gans, F., Ichii, K., Jain, A. K., Kato, E., Papale, D., Poulter, B., Raduly, B., Rödenbeck, C., Tramontana, G., Viovy, N., Wang, Y.-P., Weber, U., Zaehle, S., and Zeng, N.: Compensatory water effects link yearly global land CO<sub>2</sub> sink changes to temperature, *Nature*, 541, 516–520, <https://doi.org/10.1038/nature20780>, 2017.
- Keeling, C. D., Whorf, T. P., Wahlen, M., and van der Plicht, J.: Interannual extremes in the rate of rise of atmospheric carbon dioxide since 1980., *Nature*, 375, 666–670, <https://doi.org/10.1038/375666a0>, 1995.
- 610 King, M. P., Yu, E., and Sillmann, J.: Impact of strong and extreme El Niños on European hydroclimate, *Tellus A: Dynamic Meteorology and Oceanography*, 72:1, 1–10, <https://doi.org/10.1080/16000870.2019.1704342>, 2020.
- Kumar, A. and Hoerling, M. P.: Interpretation and implications of the observed inter-El Niño variability, *Journal of Climate*, 10(1), 83–91, [https://doi.org/10.1175/1520-0442\(1997\)010<0083:IAIOTO>2.0.CO;2](https://doi.org/10.1175/1520-0442(1997)010<0083:IAIOTO>2.0.CO;2), 1997.
- 615 Le Quéré, C., Andrew, R. M., Friedlingstein, P., Sitch, S., Hauck, J., Pongratz, J., Pickers, P. A., Korsbakken, J. I., Peters, G. P., Canadell, J. G., Arneth, A., Arora, V. K., Barbero, L., Bastos, A., Bopp, L., Chevallier, F., Chini, L. P., Ciais, P., Doney, S. C., Gkritzalis, T., Goll, D. S., Harris, I., Haverd, V., Hoffman, F. M., Hoppema, M., Houghton, R. A., Hurtt, G., Ilyina, T., Jain, A. K., Johannessen, T., Jones, C. D., Kato, E., Keeling, R. F., Goldewijk, K. K., Landschützer, P., Lefèvre, N., Lienert, S., Liu, Z., Lombardozzi, D., Metzl, N., Munro, D. R., Nabel, J. E. M. S., Nakaoka, S., Neill, C., Olsen, A., Ono, T., Patra, P., Peregon, A., Peters, W., Peylin, P., Pfeil, B.,
- 620 Pierrot, D., Poulter, B., Rehder, G., Resplandy, L., Robertson, E., Rocher, M., Rödenbeck, C., Schuster, U., Schwinger, J., Séférian, R., Skjelvan, I., Steinhoff, T., Sutton, A., Tans, P. P., Tian, H., Tilbrook, B., Tubiello, F. N., van der Laan-Luijkx, I. T., van der Werf, G. R., Viovy, N., Walker, A. P., Wiltshire, A. J., Wright, R., Zaehle, S., and Zheng, B.: Global Carbon Budget 2018, *Earth System Science Data*, 10, 2141–2194, <https://doi.org/10.5194/essd-10-2141-2018>, 2018.
- Madden, R. A.: Estimates of the natural variability of time-averaged sea-level pressure, *Monthly Weather Review*, 104(7), 942–952, [https://doi.org/10.1175/1520-0493\(1976\)104<0942:EOTNVO>2.0.CO;2](https://doi.org/10.1175/1520-0493(1976)104<0942:EOTNVO>2.0.CO;2), 1976.
- 625 Mantua, N. J. and Hare, S. R.: The Pacific Decadal Oscillation, *Journal of Oceanography*, 58, 35–44, <https://doi.org/10.1023/A:1015820616384>, 2002.
- Mantua, N. J., Hare, S. R., Zhang, Y., Wallace, J. M., and Francis, R. C.: A Pacific interdecadal climate oscillation with impacts on salmon production, *Bulletin of the American Meteorological Society*, 78(6), 1069–1080, [https://doi.org/10.1175/1520-0477\(1997\)078<1069:APICOW>2.0.CO;2](https://doi.org/10.1175/1520-0477(1997)078<1069:APICOW>2.0.CO;2), 1997.
- 630 McBride, J. L. and Nicholls, N.: Seasonal relationships between Australian rainfall and the Southern Oscillation, *Monthly Weather Review*, 111(10), 1998–2004, [https://doi.org/10.1175/1520-0493\(1983\)111<1998:SRBARA>2.0.CO;2](https://doi.org/10.1175/1520-0493(1983)111<1998:SRBARA>2.0.CO;2), 1983.
- Meehl, G. A., Washington, W. M., Arblaster, J. M., Hu, A., Teng, H., Kay, J. E., Gettelman, A., Lawrence, D. M., Sander-son, B. M., and Strand, W. G.: Climate change projections in CESM1(CAM5) compared to CCSM4, *J. Clim.*, 26, 6287–6308, <https://doi.org/10.1175/jcli-d-12-00572.1>, 2013b.
- 635 Met Office: Cartopy: a cartographic python library with a Matplotlib interface, <https://scitools.org.uk/cartopy>, address: Exeter, Devon, 2010–2015.
- Mo, K. C.: Relationships between low-frequency variability in the Southern Hemisphere and sea surface temperature anomalies, *Journal of Climate*, 13(20), 3599–3610, [https://doi.org/10.1175/1520-0442\(2000\)013<3599:RBLFVI>2.0.CO;2](https://doi.org/10.1175/1520-0442(2000)013<3599:RBLFVI>2.0.CO;2), 2000.
- 640 Monahan, A. H.: Nonlinear principal component analysis: Tropical Indo-Pacific sea surface temperature and sea level pressure, *J. Climate*, 14, 219–233, [https://doi.org/10.1175/1520-0442\(2001\)013<0219:NPCATI>2.0.CO;2](https://doi.org/10.1175/1520-0442(2001)013<0219:NPCATI>2.0.CO;2), 2001.

- Neale, R. B., Gettelman, A., Park, S., Chen, C. C., Lauritzen, P. H., Williamson, D. L., et al.: Description of the NCAR community atmosphere model (CAM 5.0), NCAR Technical Note (No. NCAR/TN-486+STR), <https://doi.org/10.5065/wgtk-4g06>, 2012.
- Newman, M., Alexander, M. A., Ault, T. R., Cobb, K. M., Deser, C., Lorenzo, E. D., Mantua, N. J., Miller, A. J., Minobe, S., Nakamura, H., Schneider, N., Vimont, D. J., Phillips, A. S., Scott, J. D., and Smith, C. A.: The Pacific Decadal Oscillation, Revisited, *Journal of Climate*, 29(12), 4399–4427, <https://doi.org/10.1175/JCLI-D-15-0508.1>, 2016.
- Pedregosa, F., Varoquaux, G., Gramfort, A., Michel, V., Thirion, B., Grisel, O., Blondel, M., Prettenhofer, P., Weiss, R., Dubourg, V., Vanderplas, J., Passos, A., Cournapeau, D., Brucher, M., Perrot, M., and Duchesnay, E.: Scikit-learn: Machine Learning in Python, *Journal of Machine Learning Research*, 12, 2825–2830, 2011.
- Peters, G. P., Minx, J. C., Weber, C. L., and Edenhofer, O.: Growth in emission transfers via international trade from 1990 to 2008, *P. Natl. Acad. Sci. USA*, 108, 8903–8908, <https://doi.org/10.1073/pnas.1006388108>, 2011b.
- Piao, S., Wang, X., Wang, K., Li, X., Bastos, A., Canadell, J. G., Ciais, P., Friedlingstein, P., and Sitch, S.: Interannual variation of terrestrial carbon cycle: Issues and perspectives, *Global Change Biology*, 26, 300–318, <https://doi.org/10.1111/gcb.14884>, 2020.
- Pittock, A. B.: Patterns of climatic variation in Argentina and Chile, I: Precipitation, 1931–60, *Monthly Weather Review*, 108, 1347–1361, [https://doi.org/10.1175/1520-0493\(1980\)108<1347:POCVIA>2.0.CO;2](https://doi.org/10.1175/1520-0493(1980)108<1347:POCVIA>2.0.CO;2), 1980.
- Pittock, A. B.: On the reality, stability and usefulness of Southern Hemisphere teleconnections, *Australian Meteorological Magazine*, 32, 75–82, [http://www.cmar.csiro.au/e-print/internal/pittock\\_x1984a.pdf](http://www.cmar.csiro.au/e-print/internal/pittock_x1984a.pdf), <http://hdl.handle.net/102.100.100/282640?index=1>, 1984.
- Poulter, B., Frank, D., Ciais, P., Myneni, R. B., Andela, N., Bi, J., Broquet, G., Canadell, J. G., Chevallier, F., Liu, Y. Y., Running, S. W., Sitch, S., and van der Werf, G. R.: Contribution of semi-arid ecosystems to interannual variability of the global carbon cycle, *Nature*, 509, 600–603, <https://doi.org/10.1038/nature13376>, 2014.
- Randall, D. A., Wood, R. A., Bony, S., Colman, T., Fichefet, T., Fyfe, J., Kattsov, V., Pitman, A., Shukla, J., Srinivasan, J., Stouffer, R. J., Sumiand, A., and Taylor, K. E.: Climate models and their evaluation, In: *Climate Change 2007: The Physical Science Basis. Contribution of Working Group I to the Fourth Assessment Report of the Intergovernmental Panel on Climate Change* [Solomon, S., D. Qin, M. Manning, Z. Chen, M. Marquis, K. B. Averyt, M. Tignor and H. L. Miller (eds.)] Cambridge University Press, Cambridge, United Kingdom and New York, NY, USA, <https://www.ipcc.ch/site/assets/uploads/2018/02/ar4-wg1-chapter8-1.pdf>, p589–662, 2007.
- Rayner, N. A., Parker, D. E., Horton, E. B., Folland, C. K., Alexander, L. V., Rowell, D. P., Kent, E. C., and Kaplan, A.: Global analyses of sea surface temperature, sea ice, and night marine air temperature since the late nineteenth century, *Journal of Geophysical Research: Atmospheres*, 108(D104), 4407, <https://doi.org/10.1029/2002JD002670>, 2003.
- Reboita, M. S., Ambrizzi, T., Crespo, N. M., Dutra, L. M. M., de S. Ferreira, G. W., Rehbein, A., Drumond, A., da Rocha, R. P., and de Souza, C. A.: Impacts of teleconnection patterns on South America climate, *Annals of the New York Academy of Sciences*, <https://doi.org/10.1111/nyas.14592>, 2021.
- Rodgers, K. B., Friederichs, P., and Latif, M.: Tropical Pacific decadal variability and its relation to decadal modulations of ENSO, *Journal of Climate*, 17, 3761–3774, [https://doi.org/10.1175/1520-0442\(2004\)017<3761:TPDVAI>2.0.CO;2](https://doi.org/10.1175/1520-0442(2004)017<3761:TPDVAI>2.0.CO;2), 2004.
- Ropelewski, C. F. and Jones, P. D.: An extension of the Tahiti–Darwin Southern Oscillation Index, *Monthly Weather Review*, 115(9), 2161–2165, [https://doi.org/10.1175/1520-0493\(1987\)115<2161:AEOTTS>2.0.CO;2](https://doi.org/10.1175/1520-0493(1987)115<2161:AEOTTS>2.0.CO;2), 1987.
- Roxy, M. K., Dasgupta, P., McPhaden, M. J., et al.: Twofold expansion of the Indo-Pacific warm pool warps the MJO life cycle, *Nature*, 575, 647–651, <https://doi.org/10.1038/s41586-019-1764-4>, 2019.

Rödenbeck, C.: Estimating CO<sub>2</sub> sources and sinks from atmospheric mixing ratio measurements using a global inversion of atmospheric transport, Technical Report 6, Max Planck Institute for Biogeochemistry, Jena, [http://www.bgc-jena.mpg.de/CarboScope/s/tech\\_report6.pdf](http://www.bgc-jena.mpg.de/CarboScope/s/tech_report6.pdf), last accessed on November 1, 2019, 2005.

Rödenbeck, C., Houweling, S., Gloor, M., and Heimann, M.: CO<sub>2</sub> flux history 1982–2001 inferred from atmospheric data using a global inversion of atmospheric transport, *Atmospheric Chemistry and Physics*, 3, 1919–1964, <https://doi.org/10.5194/acp-3-1919-2003>, 2003.

Rödenbeck, C., Zaehle, S., Keeling, R., and Heimann, M.: How does the terrestrial carbon exchange respond to inter-annual climatic variations? A quantification based on atmospheric CO<sub>2</sub> data, *Biogeosciences*, 15, 2481–2498, <https://doi.org/10.5194/bg-15-2481-2018>, 2018.

Saji, N. H. and Yamagata, T.: Possible impacts of Indian Ocean Dipole mode events on global climate, *Climate Research*, 25, 151–169, <http://www.jstor.org/stable/24868393>, 2003.

Schimel, D., Stephens, B. B., and Fisher, J. B.: Effect of increasing CO<sub>2</sub> on the terrestrial carbon cycle, *Proceedings of the National Academy of Sciences*, 112(2), 436–441, <https://doi.org/10.1073/pnas.1407302112>, 2015.

Schneider, D. P., Okumura, Y., and Deser, C.: Observed Antarctic interannual climate variability and tropical linkages, *Journal of Climate*, 25, 4048–4066, <https://doi.org/10.1175/JCLI-D-11-00273.1>, 2012.

Schneider, E. K. and Kinter, J. L.: An examination of internally generated variability in long climate simulations., *Climate Dynamics*, 10, 181–204, <https://doi.org/10.1007/BF00208987>, 1994.

Schopf, P. S. and Burgman, R. J.: A simple mechanism for ENSO residuals and asymmetry, *Journal of Climate*, 19, 3167–3179, <https://doi.org/10.1175/JCLI3765.1>, 2006.

Sheffield, J., Camargo, S. J., Fu, R., Hu, Q., Jiang, X., Johnson, N., Karaukas, K. B., Kim, S. T., Kinter, J., Kumar, S., Langenbrunner, B., Maloney, E., Mariotti, A., Meyerson, J. E., Neelin, J. D., Nigam, S., Pan, Z., Ruiz-Barradas, A., Seager, R., Serra, Y. L., Sun, D.-Z., Wang, C., Xie, S.-P., Yu, J.-Y., Zhang, T., and Zhao, M.: North American climate in CMIP5 experiments. Part II: evaluation of historical simulations of intraseasonal to decadal variability, *Journal of Climate*, 26(23), 9247–9290, <https://doi.org/10.1175/JCLI-D-12-00593.1>, 2013.

Sippel, S., Meinshausen, N., Merrifield, A., Lehner, F., Pendergrass, A. G., Fischer, E., and Knutti, R.: Uncovering the Forced Climate Response from a Single Ensemble Member Using Statistical Learning, *Journal of Climate*, 32(17), 5677–5699, <https://doi.org/10.1175/JCLI-D-18-0882.1>, 2019.

Stenseth, N. C., Ottersen, G., Hurrell, J. W., Mysterud, A., Lima, M., Chan, K.-S., Yoccoz, N. G., and Ådlandsvik, B.: Review article. Studying climate effects on ecology through the use of climate indices: the North Atlantic Oscillation, El Niño Southern Oscillation and beyond, *Proc. R. Soc. Lond. B.*, 270, 2087–2096, <https://doi.org/10.1098/rspb.2003.2415>, 2003.

Stolpe, M. B., Medhaug, I., Beyerle, U., and Knutti, R.: Weak dependence of future global mean warming on the background climate state, *Climate Dynamics*, 53, 5079–5099, <https://doi.org/10.1007/s00382-019-04849-3>, 2019.

Sun, F. and Yu, J.-Y.: A 10–15-yr modulation cycle of ENSO intensity, *Journal of Climate*, 22, 1718–1735, <https://doi.org/10.1175/2008JCLI2285.1>, 2009.

UNFCCC: National Inventory Submissions, Tech. rep., UNFCCC, <https://unfccc.int/process/transparency-and-reporting/reporting-and-review-under-the-convention/greenhouse-gas-inventories-annex-i-parties/national-inventory-submissions-2018>, last access on June 2018, 2018.

- 715 van der Werf, G. R., Randerson, J. T., Collatz, G. J., Giglio, L., Kasibhatla, P. S., Arellano Jr, A. F., Olsen, S. C., and Kasischke, E. S.: Continental-scale partitioning of fire emissions during the 1997 to 2001 El Niño/La Niña period., *Science*, 303, 73–76, <https://doi.org/10.1126/science.1090753>, 2004.
- von Storch, H.: Analysis of climate variability applications of statistical techniques, Springer-Verlag Berlin Heidelberg GmbH, <https://doi.org/10.1007/978-3-662-03167-4>, p10, 1995.
- von Storch, H. and Zwiers, W. F.: Statistical analysis in climate research, Cambridge University press, p136, 139, 1999.
- 720 Wang, K., Bastos, A., Ciais, P., Wang, X., Rödenbeck, C., Gentine, P., Chevallier, F., Humphrey, V. W., Huntingford, C., O’Sullivan, M., Seneviratne, S. I., Sitch, S., and Piao, S.: Regional and seasonal partitioning of water and temperature controls on global land carbon uptake variability, *Nature Communications*, 13, 3469, <https://doi.org/10.1038/s41467-022-31175-w>, 2022.
- Wang, X., Piao, S., Ciais, P., Friedlingstein, P., Myneni, R. B., Cox, P., Heimann, M., Miller, J., Peng, S., Wang, T., Yang, H., and Chen, A.: A two-fold increase of carbon cycle sensitivity to tropical temperature variations, *Nature*, 506, 212–215, <https://doi.org/10.1038/nature12915>, 2014.
- 725 Wills, R. C., Battisti, D. S., Hartmann, D. L., and Schneider, T.: Extracting modes of variability and change from climate model ensembles, in: Proceedings of the 7th International Workshop on Climate Informatics: CI 2017, NCAR Technical Note NCAR/TN-536+PROC, Boulder, USA, [https://climate-dynamics.org/wp-content/uploads/2017/12/ci2017\\_Wills\\_et\\_al.pdf](https://climate-dynamics.org/wp-content/uploads/2017/12/ci2017_Wills_et_al.pdf), 2017.
- Yu, J.-Y. and Kim, S. T.: Reversed spatial asymmetries between El Niño and La Niña and their linkage to decadal ENSO modulation in CMIP3 models, *Journal of Climate*, 24, 5423–5434, <https://doi.org/10.1175/JCLI-D-11-00024.1>, 2011.
- 730 Zeng, N., Mariotti, A., and Wetzol, P.: Terrestrial mechanisms of interannual CO<sub>2</sub> variability, *Global Biogeochem. Cycles*, 19, GB1016, <https://doi.org/10.1029/2004GB002273>, 2005.
- Zhu, Z., Piao, S., Xu, Y., Bastos, A., Ciais, P., and Peng, S.: The effects of teleconnections on carbon fluxes of global terrestrial ecosystems, *Geophysical Research Letters*, 44, 3209–3218, <https://doi.org/10.1002/2016gl071743>, 2017.